VORTEX DYNAMICS OF A CHANNEL WITH CAVITY FLOW

by

Antonio Cabal-Rodríguez
M.Sc., Moscow State University, Moscow, 1988

THESIS SUBMITTED IN PARTIAL FULFILMENT OF
THE REQUIREMENTS FOR THE DEGREE OF
MASTER OF SCIENCE
in the Department
of
Mathematics and Statistics

SIMON FRASER UNIVERSITY
July, 1993

Approval

Name : Antonio Cabal-Rodríguez

Degree : Master of Science

Title of Thesis : Vortex Dynamics of a Channel with Cavity Flow

Examining committee :

Chairman: *Dr. S.K.Thomason*

Dr. M.R.Trummer
Senior Supervisor

Dr. C.K.Shen

Dr. M.Singh

Dr. T.Tang
External Examiner
Department of Mathematics and Statistics
Simon Fraser University

Date Approved : July 29, 1993

PARTIAL COPYRIGHT LICENSE

I hereby grant to Simon Fraser University the right to lend my thesis, project or extended essay (the title of which is shown below) to users of the Simon Fraser University Library, and to make partial or single copies only for such users or in response to a request from the library of any other university, or other educational institution, on its own behalf or for one of its users. I further agree that permission for multiple copying of this work for scholarly purposes may be granted by me or the Dean of Graduate Studies. It is understood that copying or publication of this work for financial gain shall not be allowed without my written permission.

Title of Thesis/Project/Extended Essay

Vortex Dynamics of a Channel with Cavity Flow

Author:

(signature)

Antonio Cabal-Rodríguez

(name)

June 9th, 93

(date)

Abstract

In this thesis we study the vortex dynamics of an unsteady two dimensional viscous flow (Reynolds number 1000) in a channel with a rectangular cavity having a flow constantly entering from the left. The investigation of the generation, evolution, interactions and long-time tendency of the vortex motions is performed using a finite difference discretization of the Navier-Stokes equations in primitive variables. We follow the time development of the normalized velocity field, and study the surface and contour pressure and kinetic energy plots. A comparison between the final state of this problem and the steady state of the lid driven cavity problem is also analyzed in this work.

Dedication

To Andrea for the strength of her constant presence
and
to Tatiana for the mildness of her smile.

Acknowledgments

I would like to express my thanks to all the people who had a part in the completion of this thesis, among whom are:

My senior supervisor Dr M. R. Trummer for suggesting the topic that sprouted this work and for all his ideas and guidance. I am also deeply grateful to him for trusting my research abilities as well as for his continuous support and friendship.

Dr R. D. Russell and Dr E. Van Vleck for their readiness to help me any time I needed and for their friendship.

Dr T. Tang for our discussions, his valuable questions and comments.

Dr G. A. C. Graham and Mr P. Dobud whose personal efforts made possible my arrival to Simon Fraser University.

K. E. Korontinis, M.Sc., for his comments and corrections, especially on the first two chapters of this work, and for his invaluable friendship and support.

My family and friends whose consistent moral support helped me tremendously.

Mrs. S. Holmes for her assistance and the Department of Mathematics and Statistics of Simon Fraser University for financial support.

Contents

List of Figures

Chapter 1

Introduction

Fluid dynamics is not a young science; it has accumulated a huge amount of scientific information, theories and experimental data during the last several hundred years. However, it was not until the appearance of computers and computational fluid dynamics (CFD) that big new developments in this field took place. The continuing increase of machine speed, in part due to new massively parallel computers, as well as larger computer memories have brought the tools that may turn fluid dynamics into the central discipline of applied mathematics in the near future, as was pointed out in [20].

This thesis deals with a channel flow. During the last several decades stability properties of such flows with a vast diversity of geometries and time behavior of vortex motions have been active areas of research. In this work we are going to exhibit fascinating dynamical features of vortex motions that have not been seen in previous channel flow studies. The unsteady vortex development simulation is performed for a two dimensional incompressible laminar flow in a channel with a rectangular cavity at Reynolds number $Re = 10^3$ and a flow constantly entering from the left ($(u, v) = (1, 0)$).

We start with a review of some of the most important representative studies of

the driven cavity problem. The purpose of the review is to familiarize ourselves with various numerical methods for a problem of considerable theoretical significance. This common test problem is then used later to ensure that our numerical method of choice is working properly by reproducing a solution given in [14]. The formulation of our finite difference discretization and the boundary conditions are described in the next chapter.

To achieve a high level of accuracy we use an explicit method where a discrete Poisson's equation is solved at every time step. The third chapter briefly describes three fast direct solvers for this linear system of equations, with a more detailed description of block cyclic reduction which is used in the FISHPACK subroutine.

To give an idea of the magnitude of the computational challenge posed by these problems one should consider that the calculation of the vector field and the pressure takes approximately one second of CPU time on a SUN SPARCstation 4/670. This number is on a 60×150 grid for a single time step ($\triangle t = 10^{-3}$). The flow development was followed for 10^5 time increments.

Chapter four describes and analyzes the vortex motion of the channel problem following the four vortex dynamics stages given in [15]. A possible mesh-size dependence is investigated by running and comparing two different resolution grids. We found an unexpected transition state grid dependence that does not change the steady state. The computation of the unsteady lid driven cavity problem with the same Reynolds number and a depth/width ratio equal to 0.26 is carried out in order to compare it with the final state attained by the interior cavity of the channel problem.

Chapter 2

General Theory

2.1 Representative Work

Flow in a rectangular cavity where the motion is driven by translation of the top lid has been used as a test problem by many authors in order to check new numerical methods for fluid problems. The description below follows the summary table of some of the important representative studies given in [13].

One of the earliest papers in numerical simulation of two-dimensional Navier-Stokes (2D N-S) flows within a cavity was developed by Kawaguti [18] in 1961. In this work the author used a finite difference approximation of the vorticity-stream function formulation of the steady equations of motion. The numerical integration was performed for a small range of Reynolds numbers ($Re \leq 64$) in cavities with aspect ratio (α) equal to 0.5, 1, 2. His observations included the downstream drift of the primary vortex center with the increase of Re, in addition to the formation of corner eddies in the deep cavities ($\alpha = 2$).

Moffatt in [21] used the stream function for solving the linear steady 2D N-S Equation for small Reynolds numbers (Stokes equation). He showed a sequence of eddies of decreasing size and rapidly decreasing intensity to occur near the sharp

corners. Moffatt found theoretically that an infinite sequence of these eddies sequence exists obeying a simple similarity law.

Burggraf in [4] used a relaxation method to solve the linear steady driven cavity problem for Reynolds numbers from 0 to 400. He found that for Re greater than 100 an inviscid core developed yielding a large primary vortex near the center of the cavity, while the two secondary eddies were present in the bottom corners at all Reynolds numbers.

In 1967 Pan and Acrivos [22] produced experimental results of steady flow in rectangular cavities having finite and infinite aspect ratios for Reynolds numbers ranging from 20 to 4000. It was shown in this work that a secondary vortex in the lower right corner decreases in size as Re increases beyond 500, as well as the non-existence of a secondary vortex in the lower left corner up to Re = 2700. These two results contradict the results of many numerical experiments carried out in later work. A possible explanation for this apparent disagreement, offered in [7, 36], is that the experimental apparatus was such as to introduce vertical components of velocity at the upper boundary, owing to the use of a circular drum to form the sliding upper surface. Since the drum protruded into the cavity to about 17% of the cavity depth it was postulated that induced vertical velocities could have had an effect on the secondary vortices. The experiment was also subject to significant 3D effects, making it inappropiate as standard for comparison with the numerical solution of the 2D problem.

Bozman and Dalton [2] used a strongly implicit procedure developed by Stone [29] and compared four possibilities in representing the nonlinear terms of the 2D N-S Equations computing solutions to the cavity flow problem for a range of Re between 10 and 1000, and different grid sizes.

Benjamin and Denny [1] examined the convergence properties of various finite-differences schemes for solving the nonlinear 2D square ($\alpha = 1$) driven cavity problem at Reynolds numbers up to 10^4. In this work the existence of tertiary and fourth order corner vortices for large Re was shown. Gatski et al. [9] utilized the compact

finite difference schemes described by Rose [25] and Philips and Rose [24] to solve the vorticity-velocity form of the 2D unsteady N-S Equation. Paper [9] dealt with the dynamics to steady state of shadow and square cavity flow at Re = 400.

In Ghia et al. [10] the vorticity-stream function formulation of the 2D N-S Equations is used to study the effectiveness of the coupled strongly implicit multigrid method in the determination of high Reynolds number fine-mesh flow solutions. The driven flow in a square cavity is used as the model problem and detailed information about the streamline contours and properties of primary, secondary and terciary vortices is given with Re inceasing from 10^2 to 10^4.

Schreiber and Keller [26] used a fourth-order derivative scalar formulation of the 2D N-S Equations in terms of the stream function. To solve this equation for the square cavity problem their numerical method combines an efficient linear system solver (central differences on a uniform net yield an approximation with truncation error expansion proceeding in powers of the mesh-width square), an adaptive Newton-like method for the nonlinear system, and a continuation procedure (Keller [19]) for following a branch of solutions over a range of Re. The existence of spurious solutions for relatively coarse grids and high Re were described in detail in [27].

Gustafson and Halasi [13] studied the unsteady viscous incompressible N-S flow in a driven cavity problem with particular attention to the formation and evolution of vortices and eddies. The numerical method used by them is the projection method in a modified Marker and Cell (MAC) staggered mesh scheme. In this work the vorticity features are analyzed for cavities with α from 0.5 to 4 and Re from 10^{-6} to $2 \cdot 10^3$. In a later paper [14] the same authors analyze the dynamical features of the same problem with aspect ratio equal to 2 and at Re = 10^4. They conjecture the existence of a Hopf bifurcation at some critical Reynolds number between $2 \cdot 10^3$ and 10^4.

Goodrich et al. [11] used the time dependent stream function equation, with a Crank-Nicolson differencing scheme for the diffusion terms, and with an Adams-Bashforth scheme for the convection terms in order to solve the same problem ($\alpha = 2$) with Re = 5000. Using the relative change of the L_1 norm of the stream function per

time step, the total kinetic energy, and other scalar relations as indicators of dynamics they conjecture that the 2D N-S system of equations for the driven cavity problem with aspect ratio two possesses a Hopf bifurcation in the interval $2000 \leq \mathrm{Re} \leq 5000$.

2.2 The Navier-Stokes Equations in Primitive Variables

The motion of a continuous medium is governed by the principles of classical mechanics and thermodynamics for conservation of mass, momentum and energy. Application of these principles in a Newtonian incompressible isothermic fluid when $\mu = const$ and $\rho = const$, will give us the following dimensionless equations

$$\frac{\partial \mathbf{V}}{\partial t} + (\mathbf{V} \cdot \nabla)\mathbf{V} = -\nabla p + \frac{1}{Re}\Delta \mathbf{V}, \tag{2.1}$$

$$\nabla \cdot \mathbf{V} = 0, \tag{2.2}$$

where

$Re = \frac{UL}{\nu}$ - Reynolds number

U - reference characteristic velocity

L - reference characteristic length

$\nu = \frac{\mu}{\rho}$ - kinematic coefficient of viscosity

μ - dynamic coefficient of viscosity

ρ - density

$\mathbf{V}$ - dimensionless velocity field

p - dimensionless pressure

This system of equations is known as the dimensionless Navier-Stokes Equations.

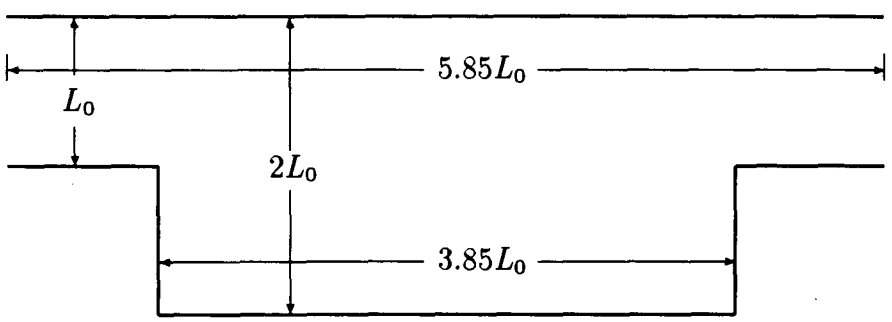

Figure 2.1: Computational domain

2.2.1 Discretization

In two dimensions the governing equations for unsteady incompressible laminar flow (written in conservative form) are

$$\frac{\partial u}{\partial t} + \frac{\partial (u^2)}{\partial x} + \frac{\partial (uv)}{\partial y} + \frac{\partial p}{\partial x} = \frac{1}{Re}\left\{\frac{\partial^2 u}{\partial x^2} + \frac{\partial^2 u}{\partial y^2}\right\}, \tag{2.3}$$

$$\frac{\partial v}{\partial t} + \frac{\partial (uv)}{\partial x} + \frac{\partial (v^2)}{\partial y} + \frac{\partial p}{\partial y} = \frac{1}{Re}\left\{\frac{\partial^2 v}{\partial x^2} + \frac{\partial^2 v}{\partial y^2}\right\}, \tag{2.4}$$

$$\frac{\partial u}{\partial x} + \frac{\partial v}{\partial y} = 0. \tag{2.5}$$

The computational domain is shown in fig. 2.1. If we denote by L_0 the dimension of the inlet height, then the width of the cavity will be $2L_0$, the cavity length will be $3.85L_0$ and the channel length will be $5.85L_0$. The characteristic length L, velocity U and time T were chosen as follow:

$L = 2L_0$ - maximum channel width

$U = U_\infty$ - inlet velocity

$T = \frac{L}{U}$

MAC Formulation

In 1965 Harlow and Welch [16] developed a technique for solving (2.3)-(2.5) that was called the Marker and Cell (MAC) method. This method with different modifications has been widely used to solve 2D N-S Equations. It uses a staggered grid and the solution of a Poisson equation for the pressure at every time-step.

The approximation of (2.3) and (2.4) is

$$\frac{u_{i+1,j}^{n+1} - u_{i+1,j}^{n}}{\triangle t} = F_{i+1,j}^{n} - \frac{p_{i+1,j}^{n+1} - p_{i,j}^{n+1}}{\triangle x}, \tag{2.6}$$

$$\frac{v_{i,j+1}^{n+1} - v_{i,j+1}^{n}}{\triangle t} = G_{i,j+1}^{n} - \frac{p_{i,j+1}^{n+1} - p_{i,j}^{n+1}}{\triangle y}, \tag{2.7}$$

while the continuity equation (2.5) is discretized as

$$D_{i,j}^{n+1} = \frac{u_{i+1,j}^{n+1} - u_{i,j}^{n+1}}{\triangle x} + \frac{v_{i,j+1}^{n+1} - v_{i,j}^{n+1}}{\triangle y} = 0. \tag{2.8}$$

In this discretization $F_{i+1,j}^{n}$ and $G_{i,j+1}^{n}$ represent the finite differencing of the combined advection and viscous terms $-(u^2)_x - (uv)_y + (u_{xx} + u_{yy})/Re$ and $-(uv)_x - (v^2)_y + (v_{xx} + v_{yy})/Re$ respectively at the nth time step i.e.

$$\begin{aligned} F_{i+1,j}^{n} = & \frac{(u_{i+1,j}^{n} + u_{i,j}^{n})^2 - (u_{i+2,j}^{n} + u_{i+1,j}^{n})^2}{4\triangle x} + \\ & \frac{(u_{i+1,j}^{n} + u_{i+1,j-1}^{n})(v_{i+1,j}^{n} + v_{i,j}^{n}) - (u_{i+1,j+1}^{n} + u_{i+1,j}^{n})(v_{i+1,j+1}^{n} + v_{i,j+1}^{n})}{4\triangle y} + \\ & \frac{1}{Re}\left[\frac{u_{i+2,j}^{n} - 2u_{i+1,j}^{n} + u_{i,j}^{n}}{\triangle x^2} + \frac{u_{i+1,j+1}^{n} - 2u_{i+1,j}^{n} + u_{i+1,j-1}^{n}}{\triangle y^2}\right], \end{aligned} \tag{2.9}$$

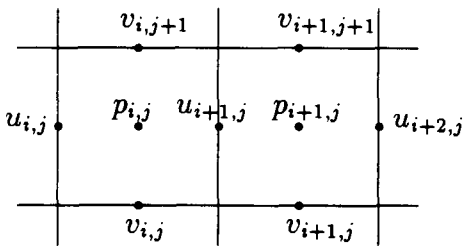

Figure 2.2: The MAC staggered grid

$$G^n_{i,j+1} = \frac{(u^n_{i,j+1}+u^n_{i,j})(v^n_{i,j+1}+v^n_{i-1,j+1})-(u^n_{i+1,j+1}+u^n_{i+1,j})(v^n_{i+1,j+1}+v^n_{i,j+1})}{4\triangle x}+$$

$$\frac{(v^n_{i,j+1}+v^n_{i,j})^2-(v^n_{i,j+2}+v^n_{i,j+1})^2}{4\triangle y}+$$

$$\frac{1}{Re}\left[\frac{v^n_{i+1,j+1}-2v^n_{i,j+1}+v^n_{i-1,j+1}}{\triangle x^2}+\frac{v^n_{i,j+2}-2v^n_{i,j+1}+v^n_{i,j}}{\triangle y^2}\right]. \qquad (2.10)$$

The staggered MAC mesh is shown in fig. 2.2

It can be seen that pressures are defined at the centre of each cell and that velocity components are defined at the midpoints of the left and right vertical boundaries for the x-directional velocity component u, and at the midpoints of the horizontal boundaries for the y-directional velocity component v.

Substitution for $u^{n+1}_{i+1,j}$, $u^{n+1}_{i,j}$, $v^{n+1}_{i,j+1}$ and $v^{n+1}_{i,j}$ from (2.6) and (2.7) into (2.8) gives a discrete Poisson equation for the pressure, i.e.

$$\frac{p^{n+1}_{i+1,j}-2p^{n+1}_{i,j}+p^{n+1}_{i-1,j}}{\triangle x^2}+\frac{p^{n+1}_{i,j+1}-2p^{n+1}_{i,j}+p^{n+1}_{i,j-1}}{\triangle y^2}=$$

$$\frac{F^n_{i+1,j}-F^n_{i,j}}{\triangle x}+\frac{G^n_{i,j+1}-G^n_{i,j}}{\triangle y}+\frac{1}{\triangle t}D^n_{i,j}. \qquad (2.11)$$

Underlying the use of these equations are assumptions that the analytic N-S Equation possesses solutions smooth enough so that they can be differentiated, continued

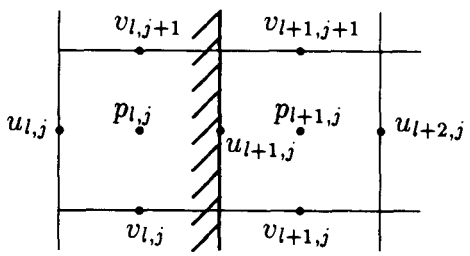

Figure 2.3: Computational cell near a vertical wall

to the boundary, and still retain a consistent discretization thereafter.

In (2.11) $\frac{D^n_{i,j}}{\Delta t}$ may be interpreted as a discretization of $-\frac{\partial D}{\partial t}\,|_{i,j}$ with $D^{n+1}_{i,j} = 0$. Thus the converged pressure solution resulting from (2.11) is such as to cause the discrete form of the continuity equation to be satisfied at time level $n+1$.

In order to solve (2.11) and then substitute the pressure into (2.6) and (2.7) to compute u and v we need to find the values of p on the boundary.

2.2.2 Pressure Boundary Conditions

The grid is arranged so that boundaries pass through velocity points but not pressure points, so in order to solve (2.11) values of the pressure outside the domain are required.

Let us take, for example, a vertical boundary. Since u at the boundary is not a function of time and since $\frac{\partial u}{\partial x} = 0$ at the wall, it follows from (2.3)

$$\frac{\partial p}{\partial x} = \frac{1}{Re}\frac{\partial^2 u}{\partial x^2} \quad , \quad \left.\frac{\partial u}{\partial x}\right|_{\partial\Omega} = 0. \tag{2.12}$$

If (2.12) is discretized at node (l,j) (see fig. 2.3) it becomes

$$\frac{p_{l+1,j} - p_{l,j}}{\Delta x} = \frac{1}{Re}\frac{u_{l+2,j} - 2u_{l+1,j} + u_{l,j}}{\Delta x^2}, \tag{2.13}$$

with

$$\frac{u_{l+2,j} - u_{l,j}}{2\triangle x} = 0 \quad and \quad u_{l+1,j} = 0, \tag{2.14}$$

or

$$p_{l,j} = p_{l+1,j} - \frac{1}{Re\triangle x} 2u_{l+2,j}. \tag{2.15}$$

Similar results are obtained for the remaining possible configurations.

2.2.3 Velocity Boundary Conditions

Consider a non-slip boundary condition for the velocity at a rigid wall. Then the normal velocities beyond the wall must be calculated in such a way as to ensure that the divergence-free condition is satisfied on the exterior cell in order to prevent $D_{i,j}$ from diffusing into the fluid. Accordingly, the conditions on u and v for the vertical case (fig. 2.3) are $u_{l,j} = u_{l+2,j}$ and $v_{l,j} = -v_{l+1,j}$, i.e. tangential velocities are simply reversed across the wall while normal velocities remain the same.

In the case when we have an inflow boundary u and v are usually given, while on an outflow boundary the typical boundary conditions would be given in such a way to keep the features of the flow at the inflow boundary.

2.2.4 Numerical Stability

According to the Lax equivalence theorem the necessary and sufficient conditions for convergence of a finite difference approximation to a given properly posed linear initial value problem are consistency and stability.

If a linearization of (2.6) and (2.7) is made (the consistency follows from the construction of the scheme) then there is a restriction on the time step for a stable solution of the explicit algorithm for u^{n+1} and v^{n+1}, namely

$$\frac{1}{4}\left(|u_0| + |v_0|\right)\triangle t Re \leq 1, \tag{2.16}$$

$$\frac{4\triangle t}{Re\triangle x^2} \leq 1 \quad where \quad \triangle x = \triangle y. \tag{2.17}$$

For more details see [23] § 6.2.3.

2.2.5 The Projection Method

An alternative MAC-like method called the projection method was proposed independently by Chorin [6] and Temam [35]. This explicit method is a fractional step method which splits into two stages:

a) Computation of the provisional vector field $\mathbf{v}^{n+1}$ - advection-diffusion component of the flow

$$\frac{\mathbf{v}^{n+1} - \mathbf{V}^n}{\triangle t} = \mathbf{F}^n. \tag{2.18}$$

b) Computation of the velocity vector at time step $n+1$ by considering the equations

$$\frac{\mathbf{V}^{n+1} - \mathbf{v}^{n+1}}{\triangle t} + \nabla p^{n+1} = 0, \tag{2.19}$$

$$\nabla \cdot \mathbf{V}^{n+1} = 0. \tag{2.20}$$

Substituting $\mathbf{V}^{n+1}$ from (2.19) into (2.20) we get the Poisson equation

$$\Delta p^{n+1} = \frac{1}{\triangle t} \nabla \cdot \mathbf{v}^{n+1}, \tag{2.21}$$

that ensures $\mathbf{V}^{n+1}$ satisfies the divergence-free equation as well as the equation of motion. In order to solve (2.19) for $\mathbf{V}^{n+1}$, (2.18) is solved for $\mathbf{v}^{n+1}$, and (2.21) for p^{n+1}. The boundary conditions for pressure and velocity are set up in the same way as shown earlier in this chapter.

In (2.19) there is an apparent dilemma of nonuniqueness that we would like to point out. If we consider the Helmholtz decomposition of the intermediate velocity field $\mathbf{v}^{n+1}$ [12]

$$\mathbf{v}^{n+1} = \mathbf{v}_1^{n+1} + \mathbf{v}_2^{n+1} + \mathbf{v}_3^{n+1},$$

where

$\mathbf{v}_1^{n+1}$ - curl-free component of $\mathbf{v}$,

$\mathbf{v}_2^{n+1}$ - divergence-free component of $\mathbf{v}$,

$\mathbf{v}_3^{n+1}$ - curl-free and divergence-free component of $\mathbf{v}$,

and three different velocity fields defined by

$\mathbf{V}_1^{n+1} = \mathbf{v}^{n+1} - \mathbf{v}_1^{n+1}$,

$\mathbf{V}_2^{n+1} = \mathbf{v}^{n+1} - \mathbf{v}_1^{n+1} - \mathbf{v}_3^{n+1}$,

$\mathbf{V}^{n+1} = \mathbf{v}^{n+1} - \triangle t \nabla p^{n+1}$,

we can notice that all these fields have the same vorticity and all are divergence-free. Any curl-free vector can be expressed as the gradient of some scalar field h, therefore $\mathbf{v}_1^{n+1} = \nabla h$, and this means

$$\Delta h = \nabla \cdot (\mathbf{v}_1^{n+1}) = \triangle t \Delta p^{n+1}.$$

The Neuman boundary condition for h is

$$\left.\frac{\partial h}{\partial \mathbf{n}}\right|_{\partial\Omega} = \mathbf{n} \cdot \mathbf{v}_1^{n+1}|_{\partial\Omega}.$$

For general domains Ω it is not clear what the values $\mathbf{n} \cdot \mathbf{v}_i^{n+1}$, i=1,2,3, should be at the boundary. However, by assuming impermeability at the boundary for the divergence-free components, $\mathbf{v}_2^{n+1}$ and $\mathbf{v}_3^{n+1}$ only, we get

$$\begin{aligned}\left.\frac{\partial h}{\partial \mathbf{n}}\right|_{\partial\Omega} = \mathbf{n} \cdot \mathbf{v}_1^{n+1}|_{\partial\Omega} &= \mathbf{n} \cdot \mathbf{v}^{n+1}|_{\partial\Omega} \\ &= \triangle t \mathbf{n} \cdot \mathbf{F}^n|_{\partial\Omega} \\ &= \triangle t \mathbf{n} \cdot \nabla p^{n+1}|_{\partial\Omega}.\end{aligned}$$

Thus $h \equiv \triangle t \cdot p^{n+1}$, and $\mathbf{V}_1^{n+1} = \mathbf{V}^{n+1}$. Similarly, under the above assumption, we see that

$$\mathbf{v}_3^{n+1} \equiv 0,$$

from which we have $\mathbf{V}_2^{n+1} = \mathbf{V}_1^{n+1} = \mathbf{V}^{n+1}$.

This analysis, given in [12], demonstrates that in order to resolve the uniqueness question for an incompressible flow simulation it is sufficient to impose an impermeability constraint on the boundary for the divergence-free component only.

The projection method as developed above coincides with the MAC method in the interior. However, the treatment of boundary conditions is slightly different.The essential difference between these two methods is that for the projection method the solution is independent of the prescription of $\mathbf{v}^{n+1}$ on the boundary, while for the MAC method it is independent of the evaluation of the normal pressure gradient on the boundary. For more details see [23] § 6.3.1 and [8] § 17.1.4.

Chapter 3

Linear Solvers

The matrices that arise from the discretization of Poisson's equation on a rectangle subject to different boundary conditions have block tridiagonal structure. The rapid solution of such systems of equations has been studied by many authors [17, 3, 5, 32, 33, 30, 31, 34, 28].

The most efficient direct algorithms for solving these systems of linear equations are the matrix decomposition method based on the fast Fourier transform (FFT), the Buneman variant of the cyclic reduction and a combination of both methods known as FACR(l) algorithm (Fourier analysis-cyclic reduction; l-number of cyclic reductions steps) [17, 31]. A brief description of these methods will be given below.

3.1 Fourier Analysis

Consider the large sparse linear system

$$A\mathbf{x} = \mathbf{b}, \tag{3.1}$$

where A is block tridiagonal with block order $m+1$

$$A = \begin{bmatrix} B & 2I & 0 & \cdots & 0 \\ I & B & I & \cdots & 0 \\ \vdots & \ddots & \ddots & \ddots & \vdots \\ 0 & \cdots & I & B & I \\ 0 & \cdots & 0 & 2I & B \end{bmatrix}, \tag{3.2}$$

and

$$\mathbf{x} = \begin{bmatrix} \mathbf{x}_0 \\ \mathbf{x}_1 \\ \vdots \\ \mathbf{x}_m \end{bmatrix} \; ; \; \mathbf{b} = \begin{bmatrix} \mathbf{b}_0 \\ \mathbf{b}_1 \\ \vdots \\ \mathbf{b}_m \end{bmatrix}. \tag{3.3}$$

The form of A given in (3.2) corresponds to the system obtained by discretizing Poisson's equation subject to Neumann boundary conditions. The matrix B is tridiagonal with scalar elements

$$B = \alpha^2 \begin{bmatrix} -2\beta & 2 & 0 & \cdots & 0 \\ 1 & -2\beta & 1 & \cdots & 0 \\ \vdots & \ddots & \ddots & \ddots & \vdots \\ 0 & \cdots & 1 & -2\beta & 1 \\ 0 & \cdots & 0 & 2 & -2\beta \end{bmatrix}_{(n+1)\times(n+1)}, \tag{3.4}$$

where α is the ratio of the spacings $\triangle y/\triangle x$ and $\beta = (1+\alpha^2)/\alpha^2$.

If we define the discrete Fourier transform $\mathbf{b}_j^\star = Q^{-1}\mathbf{b}_j$ then each of the components of $\mathbf{b}_j^\star$ i.e., $b_{q,j}^\star$, are given by

$$b_{q,j}^\star = \frac{1}{n} b_{0,j} + \frac{2}{n} \sum_{i=1}^{n-1} b_{i,j} \cos\left(qi\frac{\pi}{n}\right) + \frac{1}{n}(-1)^q b_{n,j}, \tag{3.5}$$

$$q = 0, \cdots, n \; .$$

The inverse discrete Fourier transform $\mathbf{x}_j = Q\mathbf{x}_j^\star$ is given by

$$x_{i,j} = \frac{1}{2}x_{0,j}^\star + \sum_{q=1}^{n-1} x_{q,j}^\star \cos\left(qi\frac{\pi}{n}\right) + \frac{1}{2}(-1)^i x_{n,j}^\star, \tag{3.6}$$

$$i = 0, \cdots, n \ .$$

The eigenvalues of B are

$$\lambda_q = -2\left(1 + 2\alpha^2 \sin^2\left(q\tfrac{\pi}{2n}\right)\right), \quad q = 0, \cdots, n \ . \tag{3.7}$$

Multiplying (3.1) by Q^{-1} and substituting $\mathbf{x}_j$ and $\mathbf{b}_j$ by its Fourier transform, we obtain

$$\begin{array}{rcrcrcll} Q^{-1}BQ\mathbf{x}_0^\star & + & 2\mathbf{x}_1^\star & & & = & \mathbf{b}_0^\star, & \\ \mathbf{x}_{j-1}^\star & + & Q^{-1}BQ\mathbf{x}_j^\star & + & \mathbf{x}_{j+1}^\star & = & \mathbf{b}_j^\star, & j = 1, \cdots, m-1 \\ & & 2\mathbf{x}_{m-1}^\star & + & Q^{-1}BQ\mathbf{x}_m^\star & = & \mathbf{b}_m^\star. & \end{array} \tag{3.8}$$

Then for each λ_q we obtain a system of order $m+1$

$$\begin{array}{rcrcrcll} \lambda_q x_{q,0}^\star & + & 2x_{q,1}^\star & & & = & b_{q,0}^\star, & \\ x_{q,j-1}^\star & + & \lambda_q x_{q,j}^\star & + & x_{q,j+1}^\star & = & b_{q,j}^\star, & j = 1, \cdots, m-1 \\ & & 2x_{q,m-1}^\star & + & \lambda_q x_{q,m}^\star & = & b_{q,m}^\star. & \end{array} \tag{3.9}$$

Hence, the $x_{q,j}^\star$ can easily be determined by solving a sequence of independent tridiagonal system. The solution is then given by the inverse Fourier transform $\mathbf{x}_j = Q\mathbf{x}_j^\star$.

Thus summarizing, the algorithm proceeds as follows:

- Compute or determine the eigenvalues λ_q by (3.7).
- Compute $\mathbf{b}_j^\star = Q^{-1}\mathbf{b}_j$ using (3.5).
- Solve the sequence of systems $C_q\tilde{\mathbf{x}}_q = \tilde{\mathbf{b}}_q$, where $\tilde{\mathbf{x}}_q$ and $\tilde{\mathbf{b}}_q$ are $m+1$-dimensional vectors formed with the qth components of all the $\mathbf{x}_j^\star$ and $\mathbf{b}_j^\star$, respectively; and

$$C_q = \begin{bmatrix} \lambda_q & 2 & 0 & \cdots & 0 \\ 1 & \lambda_q & 1 & \cdots & 0 \\ \vdots & \ddots & \ddots & \ddots & \vdots \\ 0 & \cdots & 1 & \lambda_q & 1 \\ 0 & \cdots & 0 & 2 & \lambda_q \end{bmatrix}_{(m+1)\times(m+1)} . \tag{3.10}$$

- Compute $\mathbf{x}_j = Q\mathbf{x}_j^*$ using (3.6).

The details of the algorithm for the remaining standard boundary conditions can be found in [31].

3.2 Block Cyclic Reduction

Given the system of linear equations (3.1) where A is defined by (3.2) and assuming that m has the form $m = 2^{k+1}$ for some integer k (the algorithm is simplified by this assumption, but such a restriction [5] has been removed [33, 34]), we have

$$\begin{aligned} B\mathbf{x}_0 + 2\mathbf{x}_1 &= \mathbf{b}_0, \\ \mathbf{x}_{j-1} + B\mathbf{x}_j + \mathbf{x}_{j+1} &= \mathbf{b}_j, \quad j = 1, 2, \cdots, m-1 \\ 2\mathbf{x}_{m-1} + B\mathbf{x}_m &= \mathbf{b}_m. \end{aligned} \tag{3.11}$$

Thus, for $j = 2, \cdots, m-2$

$$\begin{aligned} \mathbf{x}_{j-2} + B\mathbf{x}_{j-1} + \mathbf{x}_j &= \mathbf{b}_{j-1}, \\ \mathbf{x}_{j-1} + B\mathbf{x}_j + \mathbf{x}_{j+1} &= \mathbf{b}_j, \\ \mathbf{x}_j + B\mathbf{x}_{j+1} + \mathbf{x}_{j+2} &= \mathbf{b}_{j+1}. \end{aligned} \tag{3.12}$$

Multiplying the second equation of (3.12) by $-B$ and adding, we have

$$\mathbf{x}_{j-2} + (2I - B^2)\mathbf{x}_j + \mathbf{x}_{j+2} = \mathbf{b}_{j-1} + \mathbf{b}_{j+1} - B\mathbf{b}_j. \tag{3.13}$$

Thus, if j is even, the new system of equation involves $\mathbf{x}_j$'s with even indices. Similar equations hold for $\mathbf{x}_0$ and $\mathbf{x}_m$. The process of reducing the equations in this

fashion is known as *cyclic reduction.* Then (3.1) may be written as the following equivalent system:

$$\begin{bmatrix} (2I-B^2) & 2I & 0 & \cdots & 0 \\ I & (2I-B^2) & I & \cdots & 0 \\ \vdots & \ddots & \ddots & \ddots & \vdots \\ 0 & \cdots & I & (2I-B^2) & I \\ 0 & \cdots & 0 & 2I & (2I-B^2) \end{bmatrix} \begin{bmatrix} \mathbf{x}_0 \\ \mathbf{x}_2 \\ \vdots \\ \mathbf{x}_{m-2} \\ \mathbf{x}_m \end{bmatrix} = \tag{3.14}$$

$$= \begin{bmatrix} 2\mathbf{b}_1 - B\mathbf{b}_0 \\ \mathbf{b}_1 + \mathbf{b}_3 - B\mathbf{b}_2 \\ \vdots \\ \mathbf{b}_{m-3} + \mathbf{b}_{m-1} - B\mathbf{b}_{m-2} \\ 2\mathbf{b}_{m-1} - B\mathbf{b}_m \end{bmatrix},$$

and

$$\begin{bmatrix} B & 0 & \cdots & 0 \\ 0 & B & \cdots & 0 \\ \vdots & \ddots & \ddots & \vdots \\ 0 & \cdots & 0 & B \end{bmatrix} \begin{bmatrix} \mathbf{x}_1 \\ \mathbf{x}_3 \\ \vdots \\ \mathbf{x}_{m-1} \end{bmatrix} = \begin{bmatrix} \mathbf{b}_1 - \mathbf{x}_0 - \mathbf{x}_2 \\ \mathbf{b}_3 - \mathbf{x}_2 - \mathbf{x}_4 \\ \vdots \\ \mathbf{b}_{m-1} - \mathbf{x}_{m-2} - \mathbf{x}_m \end{bmatrix}. \tag{3.15}$$

Since $m = 2^{k+1}$ and the new system of equations (3.14) involves $\mathbf{x}_j$'s with even indices, the block dimension of the new system is $2^k + 1$. The system (3.14) is block tridiagonal and of the same form as (3.1), so we can apply the reduction repeatedly until we have one block.

To define the procedure recursively, let

$$B^{(0)} = B; \quad \mathbf{b}_j^{(0)} = \mathbf{b}_j; \quad j = 0, 1, \cdots, m \ .$$

Then for $r = 0, 1, \cdots, k-1$

$$\begin{aligned} B^{(r+1)} &= 2I - (B^{(r)})^2, \\ \mathbf{b}_j^{(r+1)} &= \mathbf{b}_{j-2^r}^{(r)} + \mathbf{b}_{j+2^r}^{(r)} - B^{(r)}\mathbf{b}_j^{(r)}. \end{aligned} \tag{3.16}$$

At each stage, we have a new system of equations

$$A^{(r+1)}\mathbf{x}^{(r+1)} = \mathbf{b}^{(r+1)}, \tag{3.17}$$

where

$$A^{(r+1)} = \begin{bmatrix} B^{(r+1)} & 2I & 0 & \cdots & 0 \\ I & B^{(r+1)} & I & \cdots & 0 \\ \vdots & \ddots & \ddots & \ddots & \vdots \\ 0 & \cdots & I & B^{(r+1)} & I \\ 0 & \cdots & 0 & 2I & B^{(r+1)} \end{bmatrix}, \tag{3.18}$$

and

$$\mathbf{x}^{(r+1)} = \begin{bmatrix} \mathbf{x}_0 \\ \mathbf{x}_{2^{r+1}} \\ \vdots \\ \mathbf{x}_{i2^{r+1}} \\ \vdots \end{bmatrix} \; ; \; \mathbf{b}^{(r+1)} = \begin{bmatrix} \mathbf{b}_0^{(r+1)} \\ \mathbf{b}_{2^{r+1}}^{(r+1)} \\ \vdots \\ \mathbf{b}_{i2^{r+1}}^{(r+1)} \\ \vdots \end{bmatrix} \; ; \; \begin{matrix} i = 1, 2, \cdots, 2^{k-r} - 1 \\ r = 1, 2, \cdots, k-1 \end{matrix} \tag{3.19}$$

Thus, after k steps we have the system

$$\begin{bmatrix} B^{(k)} & 2I & 0 \\ I & B^{(k)} & I \\ 0 & 2I & B^{(k)} \end{bmatrix} \begin{bmatrix} \mathbf{x}_0 \\ \mathbf{x}_{2^k} \\ \mathbf{x}_{2^{k+1}} \end{bmatrix} = \begin{bmatrix} \mathbf{b}_0^{(k)} \\ \mathbf{b}_{2^k}^{(k)} \\ \mathbf{b}_{2^{k+1}}^{(k)} \end{bmatrix}, \tag{3.20}$$

and the final reduction yields

$$[4I - (B^{(k)})^2]\mathbf{x}_{2^k} = \mathbf{b}_0^{(k)} + \mathbf{b}_{2^{k+1}}^{(k)} - B^{(k)}\mathbf{b}_{2^k}^{(k)}. \tag{3.21}$$

Note that each $B^{(r)}$ is a polynomial, say $p_{2^r}(B)$, of degree 2^r in B; then (3.21) is equivalent to writing

$$p_{2^{k+1}}(B)\mathbf{x}_{2^k} = \mathbf{b}_{2^k}^{(k+1)}. \tag{3.22}$$

Let $p_{2^{k+1}}(x)$ denote the scalar analogue of $p_{2^{k+1}}(B)$; then $p_{2^{k+1}}(x)$ will be

$$p_{2^{k+1}}(x) = 4 - [p_{2^k}(x)]^2 \tag{3.23}$$

where $p_{2^k}(x)$ is given recursively from $p_1(x) = x$ and

$$p_{2^r}(x) = 2 - [p_{2^{r-1}}(x)]^2; \quad r = 1, \cdots, k. \tag{3.24}$$

If we make the substitution $x = -2\cos\theta$, then

$$p_{2^r}(x) = -2\cos(2^r\theta),$$

or

$$p_{2^r}(x) = -C_{2^r}(x),$$

where $C_{2^r}(x)$ is the Chebyshev polynomial of degree 2^r with zeros

$$\lambda_j^{(r)} = 2\cos\left(\tfrac{(2j-1)\pi}{2^{r+1}}\right), \quad j = 1, 2, \cdots, 2^r \ . \tag{3.25}$$

Consequently,

$$p_{2^{k+1}}(x) = (2\sin(2^k\theta))^2.$$

Thus, $p_{2^{k+1}}(x) = 0$ when $x = \lambda_j^{(k+1)}$ for $j = 1, 2, \cdots, 2^{k+1}$ where

$$\lambda_j^{(k+1)} = 2\cos\left(\frac{j\pi}{2^k}\right). \tag{3.26}$$

Therefore, $p_{2^r}(B)$ can be expressed in factored form as

$$p_{2^r}(B) = -\prod_{j=1}^{2^r}(B - \lambda_j^{(r)}). \tag{3.27}$$

For $1 \leq r \leq k$, $\lambda_j^{(r)}$ is given by (3.25) and for $r = k+1$, $\lambda_j^{(k+1)}$ is given by (3.26).

We note that although B is sparse and easily inverted, the matrices $B^{(r)}$ fill rapidly; as a result the algorithm becomes expensive in terms of both storage and computation. Hence, instead of storing the matrices $B^{(r)}$, only the zeros $\lambda_j^{(r)}$ are stored, and instead of computing (3.22) we can perform all matrix computations in terms of sparse matrices using the factored form of $B^{(r)}$.

Unfortunately, the computation of the right hand sides $\mathbf{b}_j^{(r)}$ given by (3.16) is a numerically unstable process and suffers from a severe loss of significance even for relatively small values of r. To overcome this instability [5] let us define:

$$\mathbf{b}_j^{(1)} = B^{(1)}\mathbf{p}_j^{(1)} + \mathbf{q}_j^{(1)} \quad for \quad j = 0, 2, \cdots, 2^{k+1} \ ,$$

where

$$\begin{aligned}
&\mathbf{p}_0^{(1)} = B^{-1}\mathbf{b}_0, \qquad \mathbf{q}_0^{(1)} = 2(\mathbf{b}_1 - \mathbf{p}_0^{(1)}), \\
&\mathbf{p}_j^{(1)} = B^{-1}\mathbf{b}_j, \qquad \mathbf{q}_j^{(1)} = \mathbf{b}_{j-1} + \mathbf{b}_{j+1} - 2\mathbf{p}_j^{(1)}, \quad j = 2, 4, \cdots, m-2 \\
&\mathbf{p}_m^{(1)} = B^{-1}\mathbf{b}_m, \qquad \mathbf{q}_m^{(1)} = 2(\mathbf{b}_{m-1} - \mathbf{p}_m^{(1)}).
\end{aligned} \tag{3.28}$$

In general we have for $r = 1, 2, \cdots, k-1$

$$\mathbf{b}_j^{(r+1)} = B^{(r+1)}\mathbf{p}_j^{(r+1)} + \mathbf{q}_j^{(r+1)}, \tag{3.29}$$

where

$$\begin{aligned}
&\mathbf{p}_0^{(r+1)} = \mathbf{p}_0^{(r)} - (B^{(r)})^{-1}(2\mathbf{p}_{2^r}^{(r)} - \mathbf{q}_0^{(r)}), \\
&\mathbf{q}_0^{(r+1)} = 2(\mathbf{q}_{2^r}^{(r)} - \mathbf{p}_0^{(r+1)}), \\
&\mathbf{p}_j^{(r+1)} = \mathbf{p}_j^{(r)} - (B^{(r)})^{-1}(\mathbf{p}_{j-2^r}^{(r)} + \mathbf{p}_{j+2^r}^{(r)} - \mathbf{q}_j^{(r)}), \\
&\mathbf{q}_j^{(r+1)} = \mathbf{q}_{j-2^r}^{(r)} + \mathbf{q}_{j+2^r}^{(r)} - 2\mathbf{p}_j^{(r+1)}, \\
&\mathbf{p}_m^{(r+1)} = \mathbf{p}_m^{(r)} - (B^{(r)})^{-1}(2\mathbf{p}_{m-2^r}^{(r)} - \mathbf{q}_m^{(r)}), \\
&\mathbf{q}_m^{(r+1)} = 2(\mathbf{q}_{m-2^r}^{(r)} - \mathbf{p}_m^{(r+1)}).
\end{aligned} \qquad j = i2^{r+1}, i = 1, 2, \cdots, 2^{k-r} - 1 \tag{3.30}$$

Finally

$$\mathbf{b}_{2^k}^{(k+1)} = B^{(k+1)}\mathbf{p}_{2^k}^{(k+1)} + \mathbf{q}_{2^k}^{(k+1)}, \tag{3.31}$$

where

$$\begin{aligned} B^{(k+1)} &= 4I - (B^{(k)})^2 \\ \mathbf{p}_{2^k}^{(k+1)} &= \mathbf{p}_{2^k}^{(k)} - (B^{(k)})^{-1}(\mathbf{p}_0^{(k)} + \mathbf{p}_{2^{k+1}}^{(k)} - \mathbf{q}_{2^k}^{(k)}), \\ \mathbf{q}_{2^k}^{(k+1)} &= \mathbf{q}_0^{(k)} + \mathbf{q}_{2^{k+1}}^{(k)} - 4\mathbf{p}_{2^k}^{(k+1)}. \end{aligned} \tag{3.32}$$

From (3.22) we see that

$$B^{(k+1)}\mathbf{x}_{2^k} = B^{(k+1)}\mathbf{p}_{2^k}^{(k+1)} + \mathbf{q}_{2^k}^{(k+1)}, \tag{3.33}$$

so that

$$\mathbf{x}_{2^k} = \mathbf{p}_{2^k}^{(k+1)} + (B^{(k+1)})^{-1}\mathbf{q}_{2^k}^{(k+1)}. \tag{3.34}$$

Using (3.32) we can rewrite (3.34) as

$$\mathbf{x}_{2^k} = \frac{1}{4}(\mathbf{q}_0^{(k)} + \mathbf{q}_{2^{k+1}}^{(k)} - \mathbf{q}_{2^k}^{(k+1)}) + (B^{(k+1)})^{-1}\mathbf{q}_{2^k}^{(k+1)}. \tag{3.35}$$

Then, $\mathbf{x}_{2^k}$ is determined by first defining $\mathbf{z}_0 = \mathbf{q}_{2^k}^{(k+1)}$ and computing $\mathbf{z}_j$ recursively by solving a sequence of tridiagonal systems

$$(B - \lambda_j^{(k+1)}I)\mathbf{z}_j = \mathbf{z}_{j-1}, \qquad j = 1, 2, \cdots, 2^k \tag{3.36}$$

then

$$\mathbf{x}_{2^k} = \frac{1}{4}(\mathbf{q}_0^{(k)} + \mathbf{q}_{2^{k+1}}^{(k)} - \mathbf{q}_{2^k}^{(k+1)}) + \mathbf{z}_{2^k}. \tag{3.37}$$

In this manner, all computations can be performed in terms of sparse matrices. The vectors $\mathbf{q}_j^{(r)}$ are computed from (3.28) starting with

$$\begin{aligned} \mathbf{q}_j^{(0)} &= \mathbf{b}_j, && j = 0, 1, \cdots, m \\ \mathbf{q}_0^{(1)} &= 2(\mathbf{q}_1^{(0)} - B^{-1}\mathbf{q}_0^{(0)}), \\ \mathbf{q}_j^{(1)} &= \mathbf{q}_{j-1}^{(0)} + \mathbf{q}_{j+1}^{(0)} - 2B^{-1}\mathbf{q}_j^{(0)}, && j = 2, 4, \cdots, m-2 \\ \mathbf{q}_m^{(1)} &= 2(\mathbf{q}_{m-1}^{(0)} - B^{-1}\mathbf{q}_m^{(0)}). \end{aligned} \tag{3.38}$$

The remaining $\mathbf{q}_j^{(r)}$ are determined from (3.30) by

$$\begin{aligned} \mathbf{q}_j^{(r+1)} = \mathbf{q}_{j-2h}^{(r)} - \mathbf{q}_{j-h}^{(r-1)} + \mathbf{q}_j^{(r)} - \mathbf{q}_{j+h}^{(r-1)} + \mathbf{q}_{j+2h}^{(r)} + (B^{(r)})^{-1}(\mathbf{q}_{j-3h}^{(r-1)} - \\ \mathbf{q}_{j-2h}^{(r)} + \mathbf{q}_{j-h}^{(r-1)} - 2\mathbf{q}_j^{(r)} + \mathbf{q}_{j+h}^{(r-1)} - \mathbf{q}_{j+2h}^{(r)} + \mathbf{q}_{j+3h}^{(r-1)}), \end{aligned} \tag{3.39}$$

where $h = 2^{r-1}, r = 1, 2, \cdots, k-1$ and $j = i2^{r+1}, i = 1, 2, \cdots, 2^{k-r} - 1$.

The solution vectors $\mathbf{x}_j$ are given by (3.17) and (3.30)

$$\mathbf{x}_j = \frac{1}{2}(\mathbf{q}_{j-h}^{(r-1)} + \mathbf{q}_{j+h}^{(r-1)} - \mathbf{q}_j^{(r)}) + (B^{(r)})^{-1}(\mathbf{q}_j^{(r)} - \mathbf{x}_{j-2h} - \mathbf{x}_{j+2h}), \tag{3.40}$$

where $\mathbf{x}_{j-2h}$ and $\mathbf{x}_{j+2h}$ are computed at the previous step, and thus are known.

To summarize, the Buneman's block cyclic reduction algorithm proceeds as follows:

- Compute the matrices $B^{(r)}$ using (3.16) and (3.27).
- Compute the sequence of vectors $\mathbf{q}_j^{(r)}$ by (3.38) and (3.39).
- Back-solution for $\mathbf{x}_j$ using the back-substitution (3.37) and (3.40).

The details of the algorithm for the remaining standard boundary conditions can be found in [5].

3.3 Fourier Analysis - Cyclic Reduction

The FACR(l) algorithm is a combination of the two methods which have just been described. It begins with l steps of cyclic reduction in which the $\mathbf{q}_j^{(r)}$ are computed using (3.38) and (3.39) for $r = 1, \cdots, l$ where l can be chosen so as to reduce the asymptotic operation count ($l \leq k$ is yet to be determined).

With $r = l$ from (3.40) we have

$$\begin{gathered}\mathbf{x}_{j-2^l} + B^{(l)}\mathbf{x}_j + \mathbf{x}_{j+2^l} = \tfrac{1}{2}B^{(l)}(\mathbf{q}_{j-2^{l-1}}^{(l-1)} + \mathbf{q}_{j+2^{l-1}}^{(l-1)} - \mathbf{q}_j^{(l)}) + \mathbf{q}_j^{(l)}, \\ j = i2^{l+1}, i = 1, 2, \cdots, 2^{k-l} - 1\end{gathered} \tag{3.41}$$

This system can be solved using the Fourier method. Defining $\mathbf{x}_j^\star = Q^{-1}\mathbf{x}_j$, computing $\mathbf{q}_j^\star = Q^{-1}\mathbf{q}_j$ and substituting into (3.41), we obtain

$$\mathbf{x}_{j-2^l}^\star + Q^{-1}B^{(l)}Q\mathbf{x}_j^\star + \mathbf{x}_{j+2^l}^\star = \frac{1}{2}Q^{-1}B^{(l)}Q(\mathbf{q}_{j-2^{l-1}}^{\star(l-1)} + \mathbf{q}_{j+2^{l-1}}^{\star(l-1)} - \mathbf{q}_j^{\star(l)}) + \mathbf{q}_j^{\star(l)}. \tag{3.42}$$

Since $B^{(l)} = p_{2^l}(B)$, equation (3.42) reduces to $n+1$ independent tridiagonal systems of order $m/2^l - 1$,

$$x_{q,j-2^l}^\star + p_{2^l}(\lambda_q)x_{q,j}^\star + x_{q,j+2^l}^\star = \frac{1}{2}p_{2^l}(\lambda_q)(q_{q,j-2^{l-1}}^{\star(l-1)} + q_{q,j+2^{l-1}}^{\star(l-1)} - q_{q,j}^{\star(l)}) + q_{q,j}^{\star(l)}, \tag{3.43}$$

where $j = 2^l, 2 \cdot 2^l, \cdots, m - 2^l$. Once $x^*_{q,j}$ is determined from these systems then $\mathbf{x}_j$ can be obtained from the inverse transform $\mathbf{x}_j = Q\mathbf{x}^*_j$. Note, however, that only every $(2^l)th$ vector $\mathbf{x}_j$ has been determined. The remaining $\mathbf{x}_j$ are determined by l cycles of the back-substitution phase, i.e., for $r = l - 1, \cdots, 0$, using (3.40).

According to [31] the total operation count for cyclic reduction is $3mn \log_2 n$ (assuming that B is of order n) and the total asymptotic operation count for the matrix decomposition method based on the use of the FFT is $2mn \log_2 n$. In FACR(l), since l cycles of both the reduction and back-substitution are required, the count for this portion of the algorithm is $3mnl$. The Fourier analysis portion requires $2m/2^l$ transforms of length n for a count of $(mn/2^{l-1}) \log_2 n$. Hence, the total count is $3mn + 2^{1-l}mn \log_2 n$. This expression is minimized at $l = \log_2 \log_2 n + \log(\frac{2}{3} \ln 2)$ or $l \simeq \log_2 \log_2 n - 1$. Thus, we obtain an asymptotic operation count of $3mn \log_2 \log_2 n$ for the FARC algorithm.

Chapter 4

Numerical Simulation

In this chapter we are going to simulate an unsteady flow of homogeneous incompressible fluid in a channel with a cavity using the original explicit MAC method given in Section 2.2.1. The geometry of the problem and the velocity boundary conditions are shown in fig. 4.1. In all but the right open boundary the pressure boundary conditions are similar to the ones described in Section 2.2.2. On this boundary we chose $\frac{\partial p}{\partial x} = -\varepsilon$, where ε $(const)$ is the prescribed pressure gradient for Poiseuille flow. In particular, we can choose $\varepsilon = 0$; however, it must be clear that this condition is purely numerical and does not imply that the real pressure gradient is zero.

The fluid, initially at rest, is impulsively started, moving to the right because of the inlet velocity action (u,v) = (1,0). This velocity will not change throughout the continuing flow history.

The vortex dynamics of this problem was simulated for $Re = 10^3$ using a time interval $\Delta t = 10^{-3}$ and the fast direct Poisson solver HWSCRT from the FISHPACK Library to calculate the pressure field at each time step.

In order to ensure that our solution process will not lead to spurious solution we compared the 40×100 resolution with a finer grid 60×150 resolution. The detailed comparison of these two grids will be discussed below. With the same purpose and

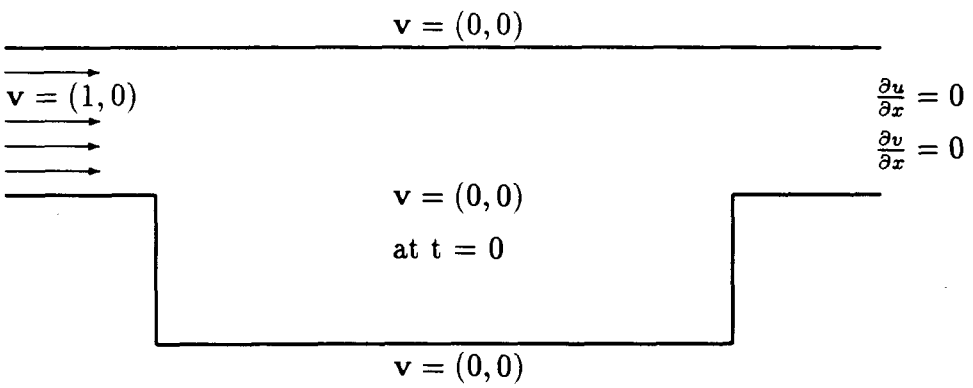

Figure 4.1: Channel with a cavity

to ensure that the code being used is working properly we computed the dynamics of the driven cavity problem for $Re = 10^4$ and $\alpha = 2$, obtaining very similar results to those of Gustafson and Halasi [14] (see fig. 4.3).

4.1 Vortex Dynamics

In the analysis of the vortex motion we are going to follow the four stages given in [15]. As it was pointed out there, these stages overlap one another throughout the flow. Nevertheless following these stages we can obtain some clarification of the flow development in terms of:

- The initial generation of the individual vortex motions.
- The basic large-scale development of vortex structures.
- The important vortex interactions.
- The long-time tendency of the vortex motions.

The discussion given below will be based on these four perspectives towards the flow development.

4.1.1 Generation of Vortex Motion

The analysis of the generation of vortex motion in a channel with a cavity at $Re = 10^3$ is carried out together with a general description of the channel flow shown in figs. 4.4, 4.5, 4.6 and 4.7. The reason why we describe these processes at the same time is because even if the flow approaches a final state, the motion generation continues throughout the flow; otherwise viscous dissipation would reduce the flow to rest.

Once the flow is impulsively started there is an immediate single recirculation at $t = 0.3sec$ on the left wall of the cavity. This left wall eddy is induced by the boundary layer separation at the left vertical wall. The causes of this boundary layer breaking are the sharp left corner and the deceleration of the oncoming flow due to the viscosity and the no-slip boundary walls. The upper left corner has acted as a provocation point.

The wall recirculation quickly becomes a clearly defined vortex (at $0.5sec$). This first appearing vortex enlarges and a counterrotating vortex forms on the lower left corner. The generation of this vortex responds to the second subprinciple (corner sequence) of the space filling principle [15], i.e. the fact that vortices try to fill a corner by generating a vortex sequence descending into it.

Meanwhile, at the upper wall of the channel there appears a well defined eddy, that acquires quickly a vortex structure, but it does not last long. After the flow enters from the left, it encounters a sudden expansion that generates a pressure drop, as shown in fig. 4.6 *c*). The decrease of the pressure expands throughout the cavity width and induces the counterrotating recirculation at the upper no-slip wall. This structure remains all the time behind the initial vortex center, it moves slowly to the right and dissipates.

Immediately after the initial vortex separates from the left wall, a similar vortex appears at the same place. This new vortex is induced by shear from the counterrotating vortex at the lower left corner, the separation of the initial vortex, the singular point and the no-slip boundary wall.

The second upper vortex gets stronger, taking energy from the main flow and

pushes the lower left corner vortex down. The last one is forced to stretch toward the bottom of the cavity and splits due to the combined action of the upper vortices.

A sequence of five of these upper left corner vortices will shed, but only the second and the fifth will survive (see the next stage). The first of the last two vortices becomes the principal vortex and it is constantly being fed energy coming from the main flow. From the sequence of the bottom vortices, it will also take "five" of them to reach its final state as a counterrotating vortex at the middle bottom of the cavity.

4.1.2 Evolution of Vortex Motion

In this second stage we will describe the history of each vortex as a single isolated structure, ignoring as much as possible the interaction with the other vortices. In other words, we are going to follow the evolution of each individual vortex motion.

We will describe our observations in a table, defining by **U** the upper vortices, follow by a number or order of appearance. The lower counterrotating vortices will be defined in a similar way by **D** and the top wall vortex by **T**. Flow evolution history is shown in figs. 4.4, 4.5, 4.6 and 4.7.

Vortex	Time	Evolution
Initial Vortex $\mathbf{U_1}$	$0.3sec$	upper left wall eddy
	$0.5sec$	left wall vortex
	$1sec$	makes contact with the cavity bottom
	$2sec$	continues strengthening and stretching toward the center of the cavity
	$3sec$	strong enough to begin inducing $\mathbf{D_1}$ in the lower left corner
	$8sec$	separates from the left wall, is covering almost the whole interior of the cavity

	$9sec$	reaches the lower right corner as well as the right wall
	$12sec$	pushed into smaller area due to the rise of $\mathbf{U}_2$ and $\mathbf{D}_{12}$
	$14sec$	is getting smaller and weaker (dissipating)
	$15sec$	about to be absorbed (the remaining portion) into $\mathbf{U}_2$, strengthening the latter
	$16sec$	gone
Principal Vortex $\mathbf{U}_2$	$8sec$	new recirculating core induced by the separation of $\mathbf{U}_1$ from the left wall, combined with the action of $\mathbf{D}_1$ and no-slip wall
	$10sec$	acquires vortex structure
	$11sec$	continues strengthening and pushes $\mathbf{D}_1$ down, forcing the last one to split
	$12sec$	stretches toward the center and the bottom of the cavity
	$13sec$	moves into the interior of the cavity
	$15sec$	is about to absorb $\mathbf{U}_1$
	$16sec$	makes contact with the left wall
	$18sec$	has reached its final position, to play the role for the rest of the flow history as the primary right recirculation
Secondary Vortex $\mathbf{U}_3$	$13sec$	well defined eddy induced by the separation of $\mathbf{U}_2$ from the left wall
	$15sec$	stretches toward the center of the cavity
	$18sec$	fully formed fast strengthening vortex
	$19sec$	has reached the bottom of the cavity
	$20sec$	clearly leaving the left wall dynamics
	$21sec$	has been absorbed by $\mathbf{U}_2$ (gone)

Secondary Vortex $\mathbf{U_4}$	$20sec$	has been induced by the same source as $\mathbf{U_2}$ and $\mathbf{U_3}$
	$21sec$	strong enough to influence the split of $\mathbf{D_{111}}$
	$23sec$	makes contact with the cavity bottom and separates into the interior
	$24sec$	has pushed $\mathbf{U_2}$ into smaller area
	$25sec$	is weakening, will compete with $\mathbf{U_2}$
	$26sec$	has been absorbed by $\mathbf{U_2}$ (gone)
Secondary Vortex $\mathbf{U_5}$	$23sec$	upper left wall eddy
	$26sec$	is stretching slowly toward the center (still a very narrow recirculation)
	$27sec$	expands rapidly due to the vanishing of $\mathbf{U_4}$ rivalry
	$28sec$	appears to have an unsuccessful attempt of separation from the left wall (at least in the current grid resolution)
	$31sec$	is about to reach its final state structure, to become the main upper left (large and narrow) cavity vortex
Secondary Vortex $\mathbf{D_1}$ - - - - - - - $\mathbf{D_{12}}$	$3sec$	counterrotation induced by $\mathbf{U_1}$
	$6sec$	well defined lower left corner vortex
	$8sec$	continues strengthening, occupies most of the region left by $\mathbf{U_1}$ at separation
	$10sec$	is pushed down by $\mathbf{U_2}$
	$11sec$	splits ($\mathbf{D_{11}}$ and $\mathbf{D_{12}}$) due to the combined action of $\mathbf{U_1}$ and $\mathbf{U_2}$
	$12sec$	occupies the middle bottom part of the cavity and is moving fast to the right
	$13sec$	is weakening
	$15sec$	is gone, mostly dissipated

Secondary	12*sec*	lower left corner vortex
Vortex	16*sec*	stretches toward the bottom of the cavity
$\mathbf{D}_{11}$	18*sec*	is forced to split ($\mathbf{D}_{111}$ and $\mathbf{D}_{112}$)
- - - - - - -	19*sec*	well formed middle bottom vortex
$\mathbf{D}_{112}$	20*sec*	is dissipating fast
	21*sec*	gone
Secondary	19*sec*	well defined bottom vortex
Vortex	21*sec*	is breaking up into $\mathbf{D}_{1111}$ and $\mathbf{D}_{1112}$
$\mathbf{D}_{111}$	22*sec*	a tertiary recirculation appears between the new two
- - - - - - -		vortices, but it cannot compete
	23*sec*	middle bottom vortex
$\mathbf{D}_{1112}$	24*sec*	is weakening, about to disappear
	25*sec*	gone
	23*sec*	well formed bottom eddy
Secondary	24*sec*	has stretched toward the bottom
Vortex	25*sec*	well defined vortex
$\mathbf{D}_{1111}$	26*sec*	is about to split
	27*sec*	a barely organized recirculation structure is spawned
- - - - - - -		between $\mathbf{D}_{11111}$ and $\mathbf{D}_{11112}$ but it will not last long
	28*sec*	left bottom eddy
$\mathbf{D}_{11111}$	30*sec*	appears to fuse with $\mathbf{D}_{11112}$
	32*sec*	has split again, now it is a very weak structure, about
		to disappear
	33*sec*	gone
	32*sec*	fully formed vortex after the last fission of $\mathbf{D}_{1111}$
$\mathbf{D}_{11112}$	33*sec*	has survived, to become the main counterrotating
		structure of the steady state

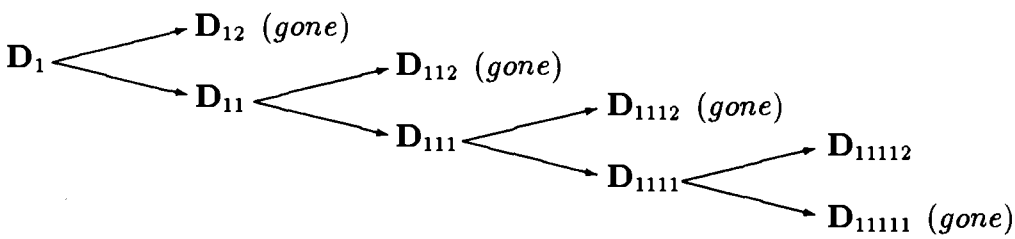

Figure 4.2: $\mathbf{D}_1$ fission process

Secondary Vortex $\mathbf{T}_1$	$2sec$	top wall eddy induced by the drop of the pressure behind the initial vortex, as well as the no-slip top wall
	$3sec$	well formed wall vortex
	$4sec$	is strengthening and moving to the right pushed by the main flow
	$6sec$	begins to dissipate
	$7sec$	fully dissipated
Wall Eddy $\mathbf{T}_2$	$14sec$	the pressure depression generated by $\mathbf{U}_2$ reaches the top wall of the channel, inducing a counterrotation
	$16sec$	gone

In order to bring a better idea of the $\mathbf{D}_1$ sequence of splits a graphic of the fission process is shown in fig. 4.2

The evolution of a fluid flow and its dynamics are very interrelated concepts, so the next natural step is to describe the flow dynamics.

4.1.3 Dynamics of Vortex Motion

The main objective here is to emphasize the role of vortex interaction. We do not pretend to formulate any general principle of such a vast and complex subject as vortex motion dynamics; all we are going to do is to describe some aspects of the

dynamics of the studied flow.

If we look at the initial dynamics of the problem we can realize that the initial vortex, and as a consequence the vortex dynamics of the flow, starts due to the action of the viscous term in the boundary layer near the left vertical wall, i.e. it has a viscous origin. Part of the translational motion energy of the instantaneously created inlet flow is transferred to rotational motion in order to preserve the continuity of the fluid behind the separation point.

The amount of rotational energy transfer to the fluid near the left corner of the vertical cavity wall is sufficient to make possible the generation of a fully organized small vortex motion which then continues to grow (energy is constantly fed into it by the main flow) and accelerates until it separates from the lower left corner inducing a counterrotating recirculation. This new rotational motion acquires its vortex structure very fast due to the energy provided by $\mathbf{U}_1$ but at the same time with its growth and strengthening $\mathbf{D}_1$ will contribute to the separation of the initial vortex from the left wall.

An interesting feature of this problem are the pair interactions $\mathbf{U}_2 \leftrightarrow \mathbf{U}_1$ and $\mathbf{U}_i \leftrightarrow \mathbf{U}_2$ ($i = 3, 4$ *and* 5). All these pairs survive just as long as the opposite-signed vortex between them is alive; once the latter disappears (mostly through dissipation) a fusion process begins. In the case of $\mathbf{U}_2 \leftrightarrow \mathbf{U}_1$, the second one is not strong enough to stop the advance of $\mathbf{U}_2$ that will weaken, reduce and then absorb $\mathbf{U}_1$ (see fig. 4.5 (I) $t = 15sec$ and (II) $t = 16sec$).

For the next two pairs ($\mathbf{U}_3 \leftrightarrow \mathbf{U}_2$ and $\mathbf{U}_4 \leftrightarrow \mathbf{U}_2$) the left hand side vortex will compete, pushing $\mathbf{U}_2$ into a smaller area, but $\mathbf{U}_2$ will finally win in the fusion process, absorbing the oncoming vortices. The last pair $\mathbf{U}_5 \leftrightarrow \mathbf{U}_2$ will reach a stable state ($t = 33sec$) together with $\mathbf{D}_{11112}$ forming a trio that will last for the rest of the flow history.

The $\mathbf{D}_1$ split sequence dynamics is based on the strain induced by the recent growing upper left corner vortex combined with the action of the respective right hand side vortex. The first one pushes the corresponding $\mathbf{D}_1$ sequence vortex down

and forces it to stretch. Meanwhile the vortex on the right keeps transferring energy to it, so at one point this counterrotating vortex has to break up in order to satisfy the requirements of the two vortices that are energetically feeding it, i.e. it has to play the role of the opposite-signed vortex between the upper pair and to cover the lower left corner of the cavity.

Finally, looking at the flow entering from the left we find out that after $11sec$ it behaves almost the same way as if this was a problem of a flow in a straight channel (see fig. 4.5 (I)). In other words, once the vortex motions of the flow have filled up all the cavity space, this region acts as a closed domain, having very little mixing between the main flow and the flow inside the cavity. Hence, we can conclude that the flow itself changes the effective geometry of the problem, using the constantly entering flow just as an energetic supplier.

4.1.4 Limits of Vortex Motion

We have reached the point were a conclusion about the flow's final state has to be made. Looking at the development of the physical magnitudes such as kinetic energy, pressure and velocity vector field it is clear that the steady state has been attained at approximately $t = 40sec$ (see figs. 4.5 (IV), 4.6 (III) and 4.7 (III)).

The fundamental features of this state are two counterclockwise vortices and one vortex with the opposite direction. The momentum scale for the inside flow (fig. 4.7 (III)) shows the highest concentration of energy in the cavity located on the right hand side of it. This energy is mainly coming from the flow constantly entering from the left. The inside flow that is moving along with the previous one hits the right wall close to the upper corner and divides into two streams; one goes down the cavity and the other leaves in the opposite direction to join the channel flow. The high pressure located close to the upper right corner of the cavity shown in fig. 4.6 (III) confirms the existence of a stagnation point at the place where the flow splits.

As we can see in fig. 4.7 (III) there is a very uniform and almost dead region on

the lower left side of the cavity. During the basic energy distribution process that has taken place in the first stage of the vortex dynamics, the amount of energy the inner flow has at its disposal is not enough to feed any recirculation on the lower left side of the cavity domain, so in this region the already limited movement is very slow.

Neither the coarse grid nor the finer grid simulation clarifies the situation in the lower left corner. There both, the pressure and the kinetic energy surfaces appear to have singularities. It seems that a very fine grid simulation is needed in order to decide whether there exists some kind of recirculation or this is just a stagnation point.

Notice that the kinetic energy hill rising just in the cavity-channel boundary responds to the parabolic distribution of the problem of a flow in a channel with two parallel flat walls (see fig. 4.7 (III)). This corroborates the fact that vortex dynamics inside the cavity has transformed the geometry of the problem, generating a closed region under the main flow.

4.2 Coarse Grid vs. Finer Grid

In the previous section we have analyzed in detail the dynamics of the two dimensional flow in a channel with a rectangular cavity having a uniform mesh-size with grid spacing equal to $1/60$ on both x and y directions. Before we have started working on this problem, and in order to investigate possible mesh-size dependence we ran the same problem on a coarser grid with a uniform grid spacing equal to $1/40$ (see fig. 4.8).

One of the most interesting differences between these two grids is the fact that in the coarse grid $\mathbf{U}_3$ instead of $\mathbf{U}_2$ plays the role of the principal vortex covering the right hand side of the cavity. On the other hand $\mathbf{U}_1$ incorporates $\mathbf{U}_2$ (see fig. 4.8 (II) *e*) and *f*)) into itself to be absorbed later by $\mathbf{U}_3$ at $t = 26sec$; so in this respect the upper sequence order also changes.

The $\mathbf{D}_1$ sequence of splits is hard to follow on the coarse grid and at some points

it is barely defined. This is not the case with the top channel recirculation $\mathbf{T}_1$, which seems to be stronger than the corresponding one on the finer grid and it lasts longer (see fig. 4.8 (I)).

Summarizing we can say that independently of the vortex evolution, differences between the coarse and the finer mesh-sizes, the final states of both grids are qualitatively the same. At $t \approx 40$ for the finer grid and $t \approx 50$ for the coarse grid the steady states features of both flows are essentially the same.

4.3 Final Remarks

Without going into any vortex dynamics details of the unsteady driven cavity problem for $Re = 10^3$ and $\alpha = 0.26$, we are going to compare the steady state of this problem with the final state reached by the interior domain in the channel with a cavity flow.

Fig. 4.9 shows the existence of a right hand side recirculation on a driven cavity problem quite similar to the principal vortex $\mathbf{U}_2$ in the channel problem, even though the lower right corner vortex seen in this figure is not clear in either of the two above analyzed different mesh resolutions for the channel flow. Looking to the momentum scale of both problems (see fig. 4.11) we find out that it is mostly concentrated on the right side of the domain, having a very uniform flat distribution in the opposite region.

Independently of the fact that pressure and kinetic energy distributions (see figs. 4.10 and 4.11) are qualitatively quite similar in the steady state of both problems, we should point out the drastic change of the vortex motion on the left part of the driven cavity flow (see fig. 4.9 *b*)). There is a well defined counterrotating vortex covering three quarters of the left cavity wall, where the channel flow used to have a "movement" in the opposite direction. The bottom counterrotation $\mathbf{D}_{11112}$ has disappeared in the cavity problem and what used to be an upper large vortex ($\mathbf{U}_5$) has become a very narrow and barely defined recirculation in this problem.

Finally, we have to mention the interesting fact that the differences between these

two problems with $Re = 10^3$ will disappear for $\alpha = 0.5$ or $\alpha = 1$. For these depth/width ratios of the interior cavity the channel with a cavity has essentially the same steady state as the corresponding driven cavity problem.

4.4 Conclusions

During the last few years vortex dynamics has been an active area of research. Vortex methods have been applied to a vast variety of fluid flow problems with industry and nature as constant suppliers of new challenges in this field, but so far a complete theory of vortex dynamics has not been developed.

The main objective of this thesis is to describe and analyze different aspects of the generation, evolution, interaction and long-time tendency of the vortex motion in one particularly interesting two dimensional unsteady viscous problem: *a channel with cavity flow.* Our numerical results can be summarized as follow:

- On the coarse grid all calculations indicate that the solution attains a steady state at $t \approx 50sec.$ This state is characterized by a main "straight channel flow" and a closed domain with a trio of a right principal vortex, an upper large left vortex and a middle bottom counterrotating recirculation.
- On the finer grid all calculations indicate that the solution attains a steady state for $t \approx 40sec.$ This state is characterized by a main "straight channel flow" and a closed region with a principal vortex covering more than one third of the cavity (right part), an upper left vortex and a counterrotating vortex at the middle bottom.
- On the lid driven cavity problem all calculations indicate that the steady state attained by the solution is different from the final state reached by the refined grid channel problem, specially on the left side. This is not the case for similar comparisons when $\alpha = 0.5$ and $\alpha = 1$.

Several interesting flow dynamics have also been shown by simulating the normalized velocity field during the flow history. The $\mathbf{D_1}$ fission sequence and the upper vortex pair interactions are two particularly good examples of these dynamics.

The grid dependence seen in the transition state could be due to the filtration of smaller scale dynamic processes, but the interesting result is the fact that these unexpected differences did not affect the final states reached by both grids, which are essentially the same. These results show that this problem has still some open questions and suggest the necessity of further study.

We believe this research will help in a better understanding of the vortex motion nature and will give rise to new interesting questions in this field. The vortex dynamics of the unsteady driven cavity problems at $Re \geq 5 \cdot 10^3$ and $\alpha \leq 1/3$ is an interesting open problem, and work on this problem is in progress.

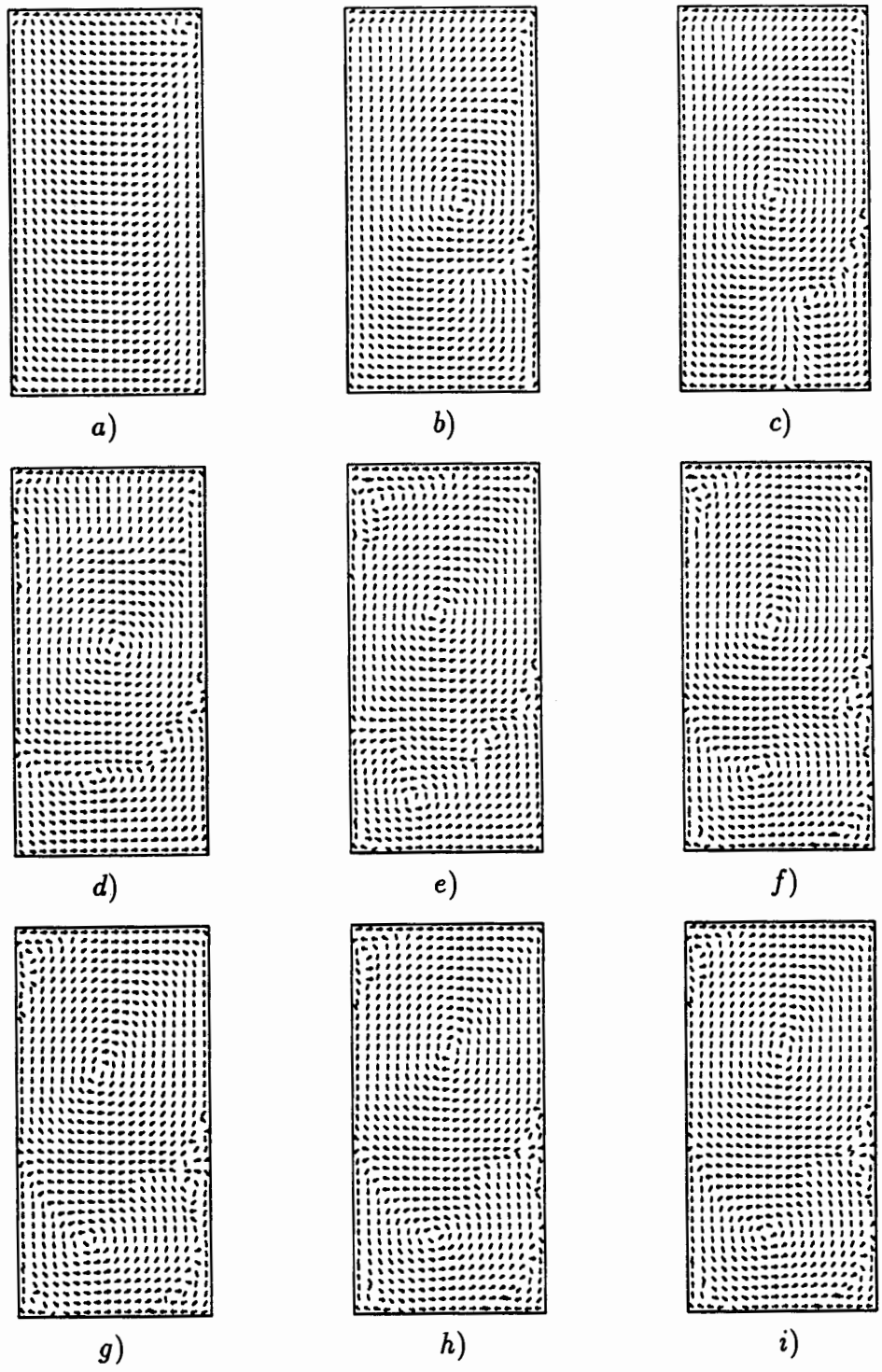

Figure 4.3: Normalized velocity field in a lid driven cavity flow ($Re = 10^4, \alpha = 2$), at : *a*) $t = 2$, *b*) $t = 18$, *c*) $t = 25$, *d*) $t = 34$, *e*) $t = 52$, *f*) $t = 70$, *g*) $t = 96$, *h*)

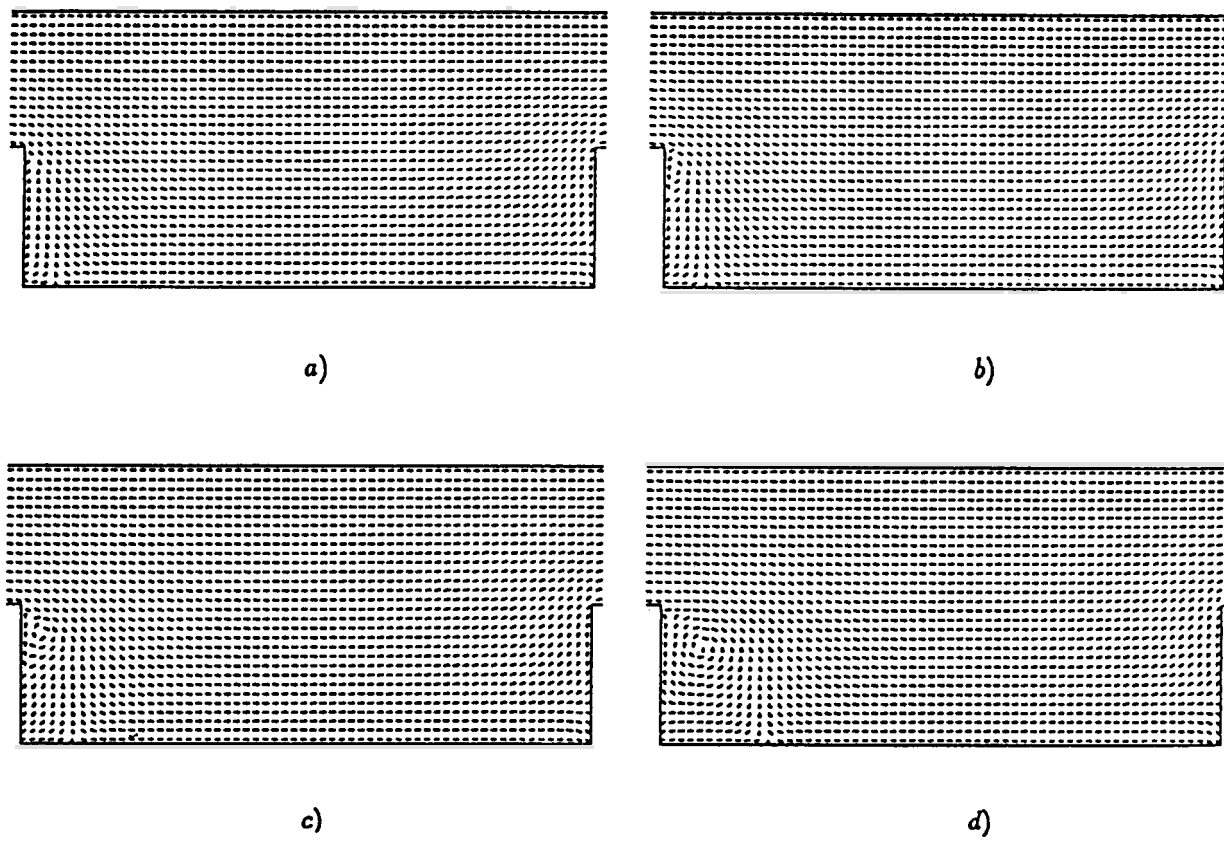

Figure 4.4: (I) Time-development of the unsteady normalized velocity field in a channel with a cavity flow ($Re = 10^3$) at *a*) $t = 0.1sec$, *b*) $t = 0.3sec$, *c*) $t = 0.5sec$ and *d*) $t = 1sec$.

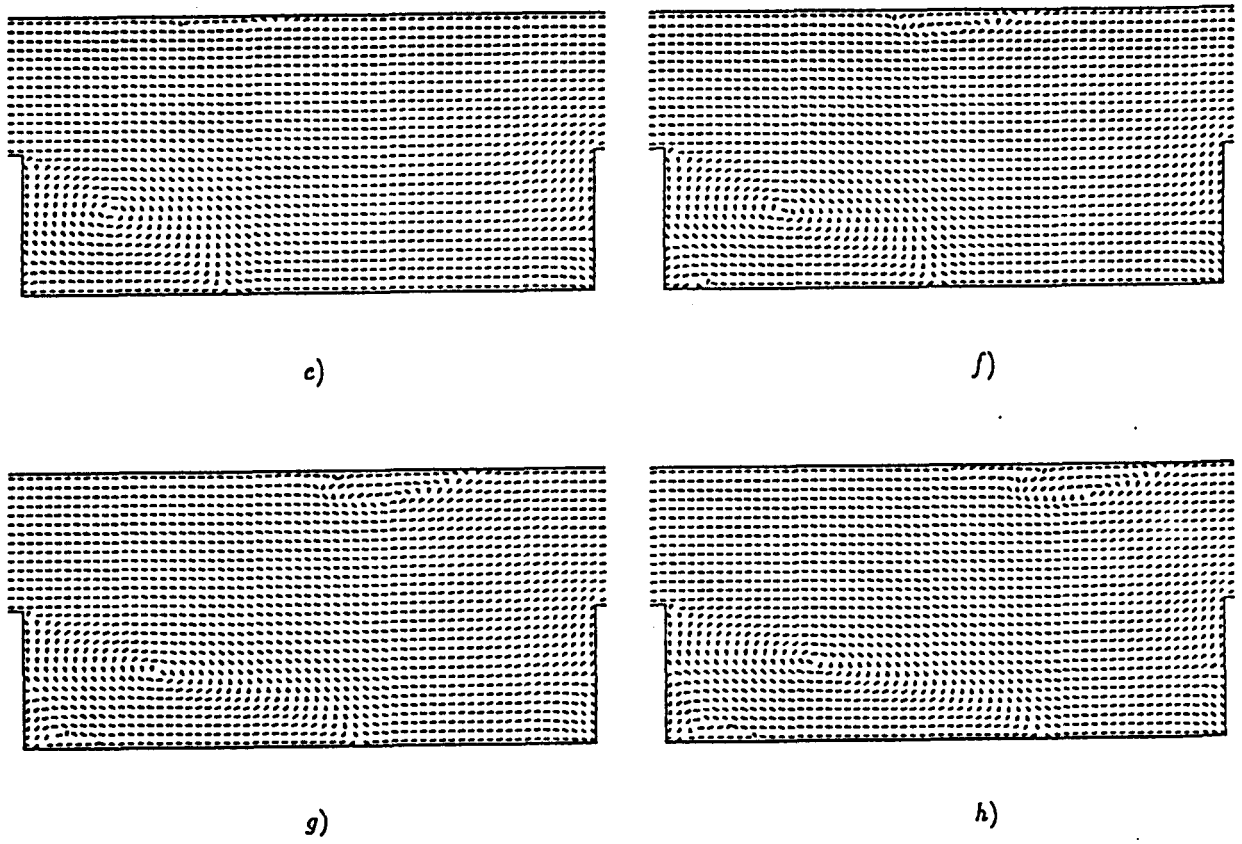

Figure 4.4: (II) from $t = 2sec$ to $t = 5sec$ at one second intervals moving to the right.

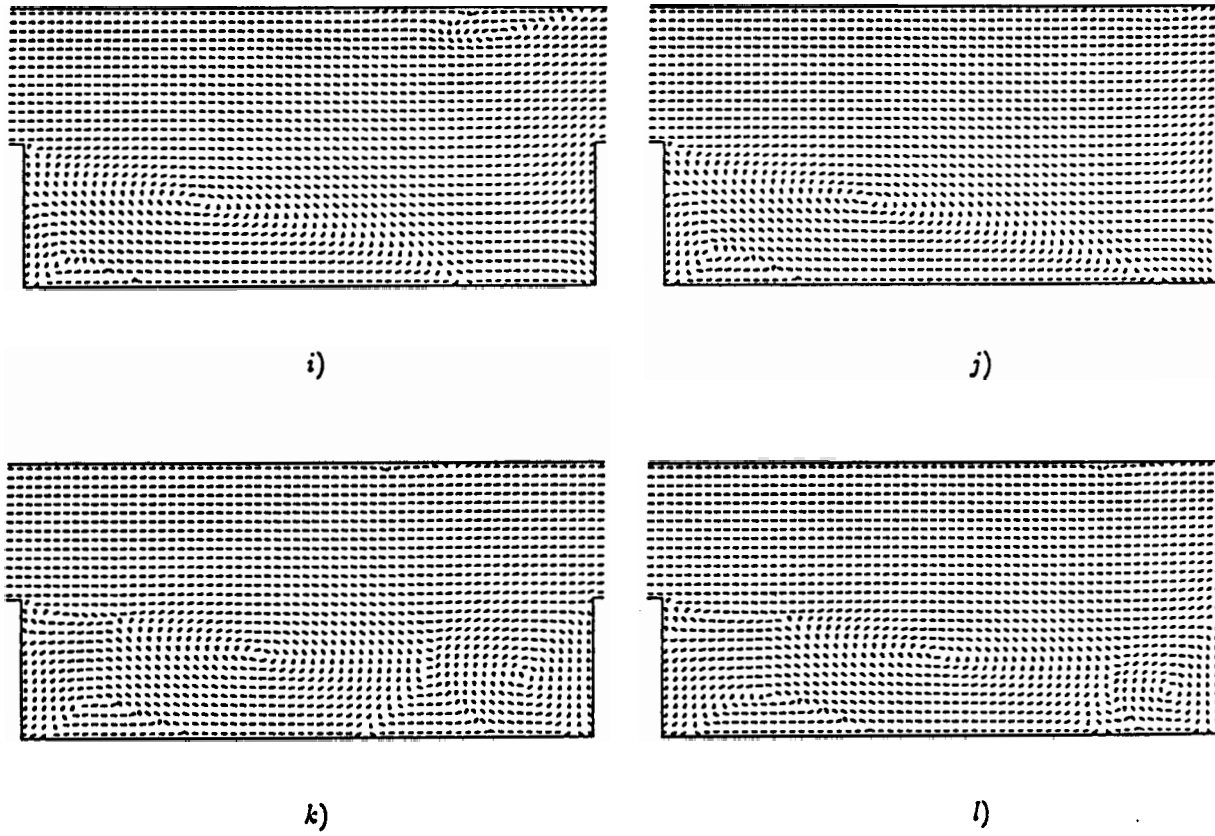

Figure 4.4: (III) $i)$ $t = 6sec$, $j)$ $t = 7sec$, $k)$ $t = 14sec$ and $l)$ $t = 15sec$.

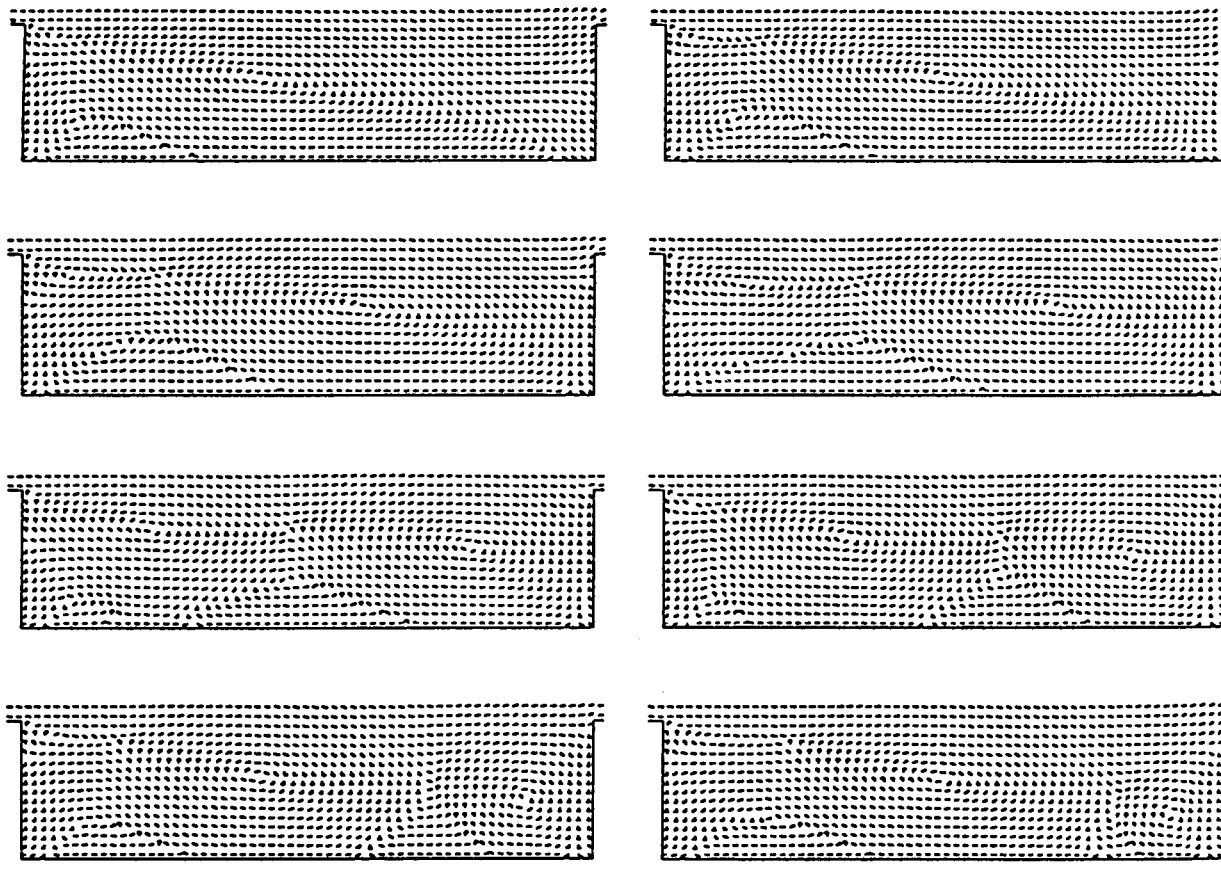

Figure 4.5: Time-development of the unsteady normalized velocity field in the bottom half of the domain ($Re = 10^3$) from (I) $t = 8sec$ to $t = 15sec$ at one second intervals moving to the right.

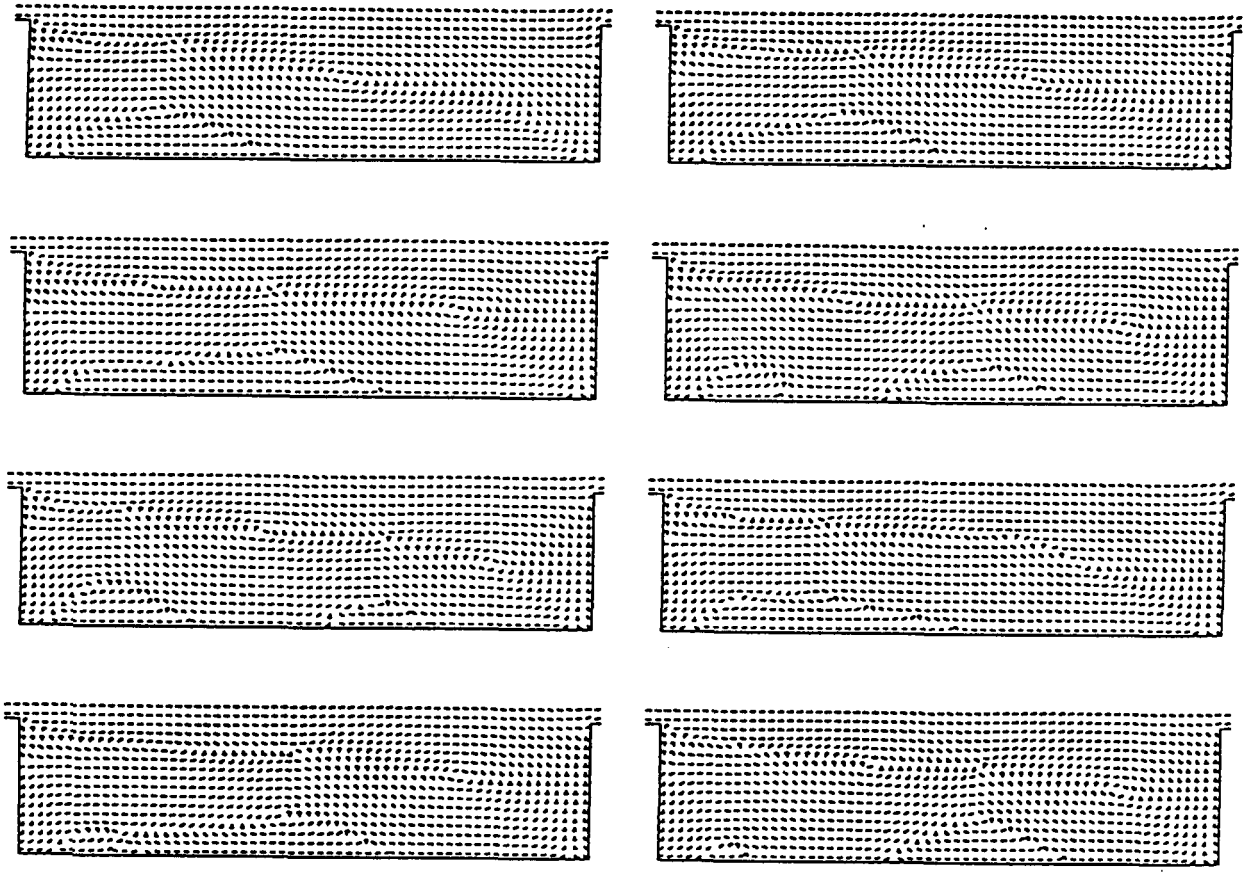

Figure 4.5: (II) $t = 16sec$ to $t = 23sec$.

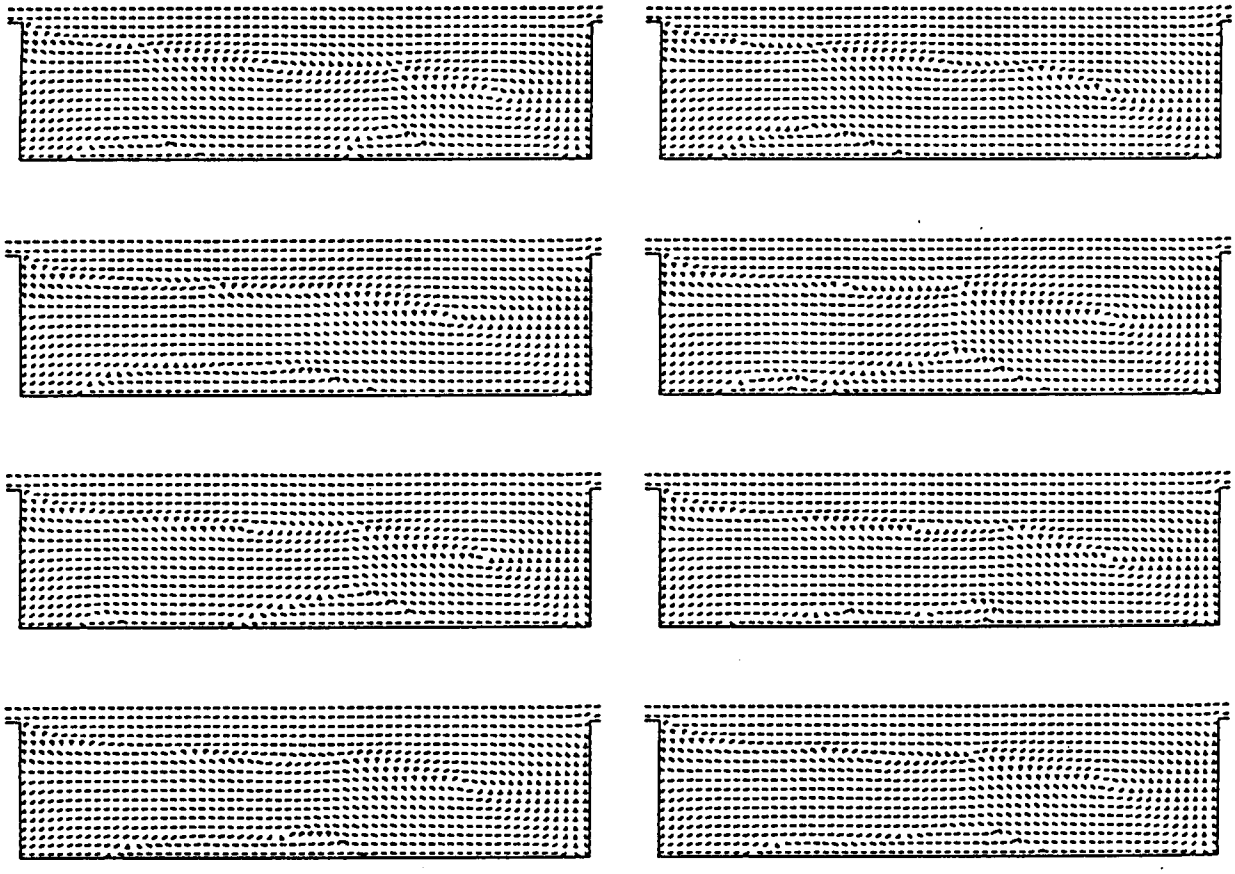

Figure 4.5: (III) $t = 24sec$ to $t = 31sec$.

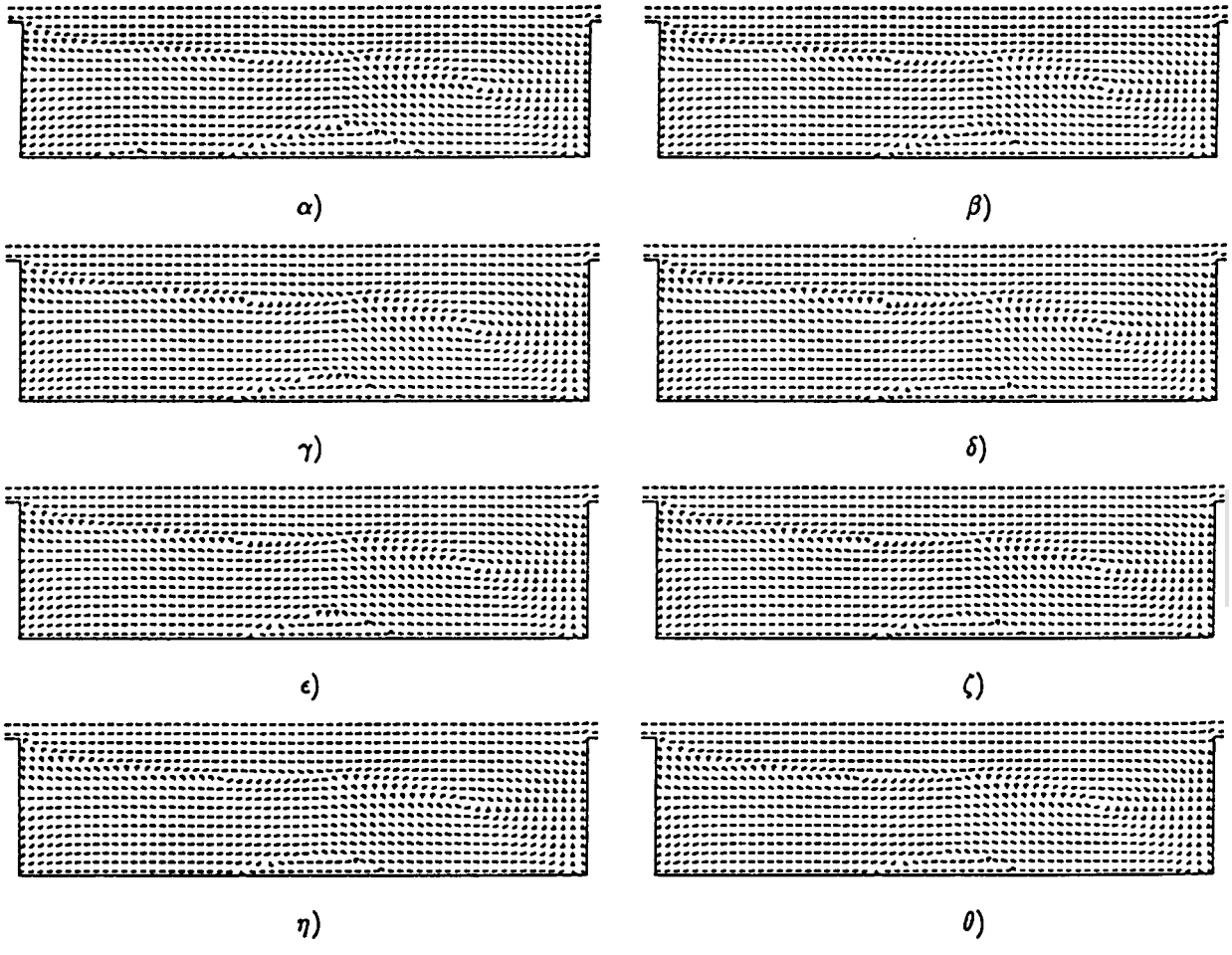

Figure 4.5: (IV) $\alpha)$ $t = 32sec$ to $\delta)$ $t = 35sec$ at one second intervals; $\epsilon)$ $t = 38sec$, $\zeta)$ $t = 40sec$, $\eta)$ $t = 60sec$ and $\theta)$ $t = 100sec$.

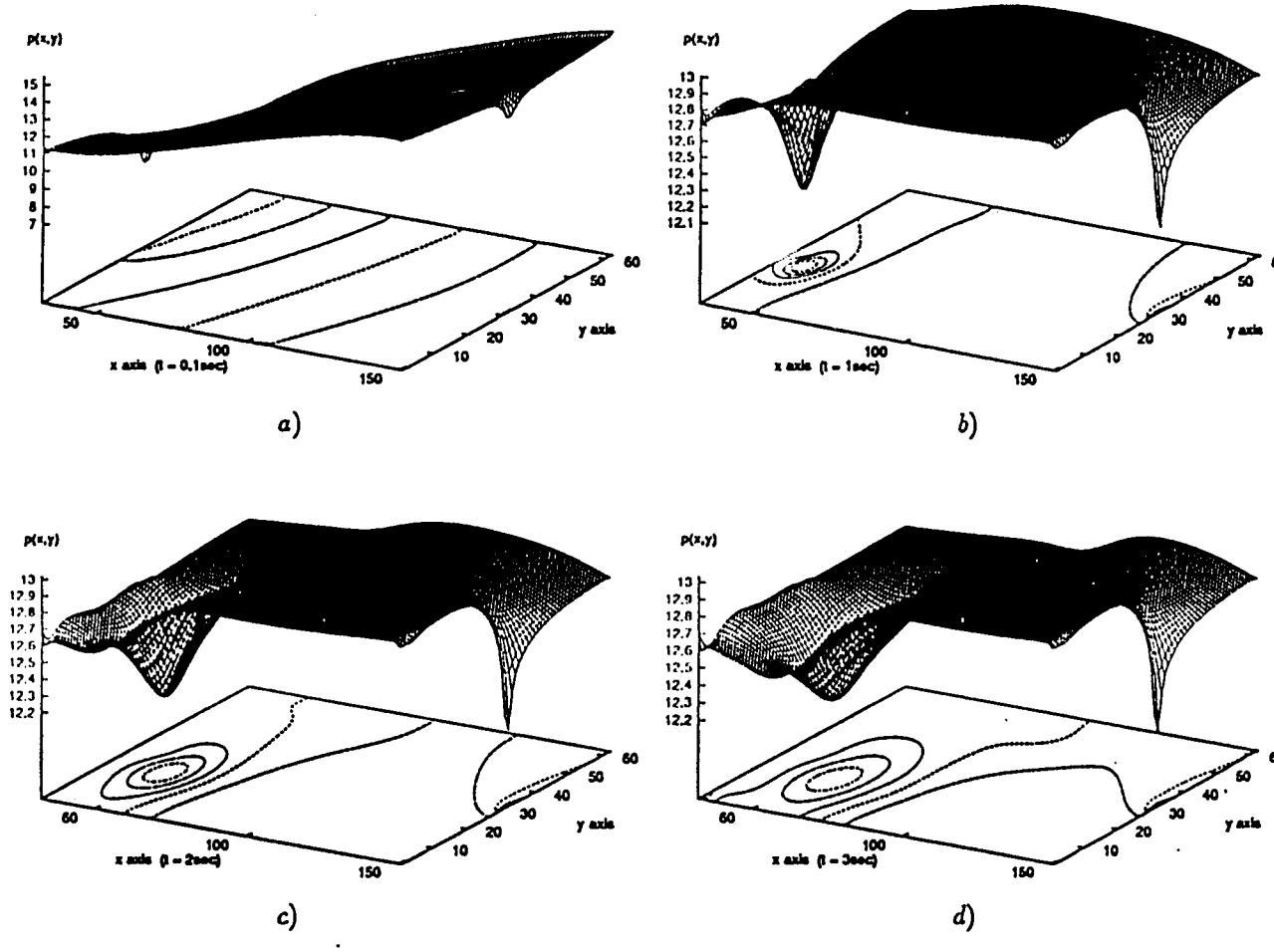

Figure 4.6: Time-development surface and contour plot of pressure ($Re = 10^3$) at (I) *a*) $t = 0.1scc$, *b*) $t = 1scc$, *c*) $t = 2scc$ and *d*) $t = 3scc$

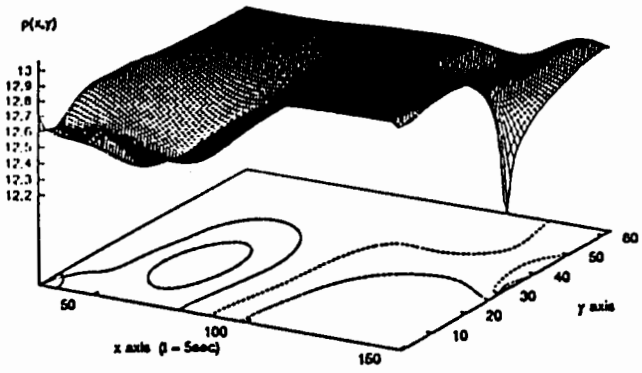

c)

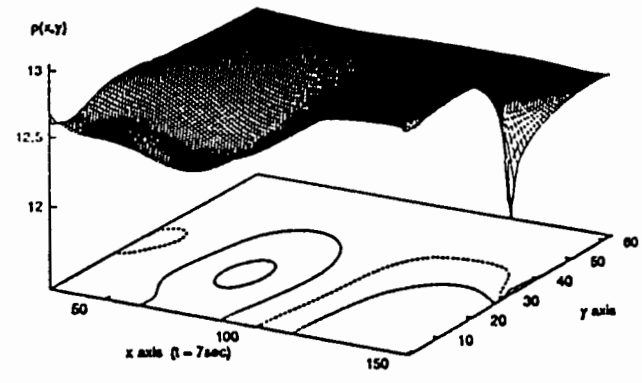

f)

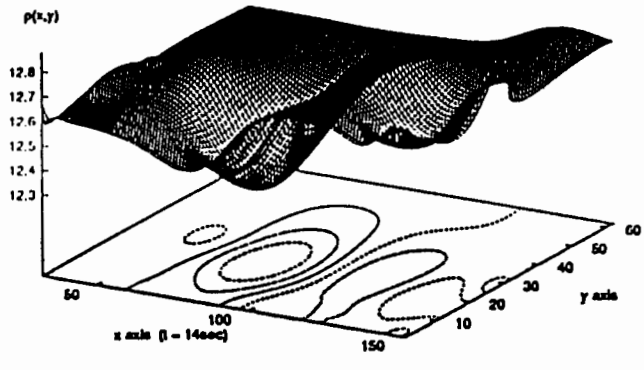

g)

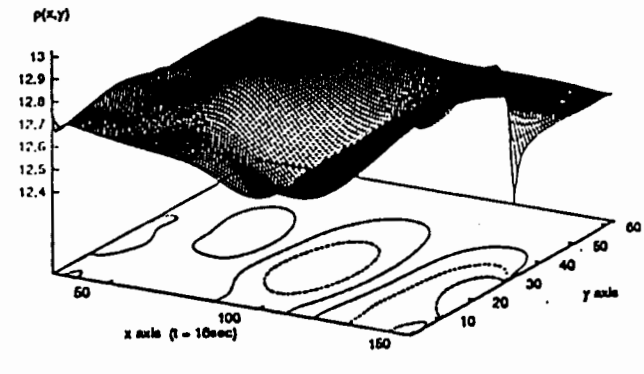

h)

Figure 4.6: (II) *c)* $t = 5sec$, *f)* $t = 7scc$, *g)* $t = 14sec$ and *h)* $t = 16sec$

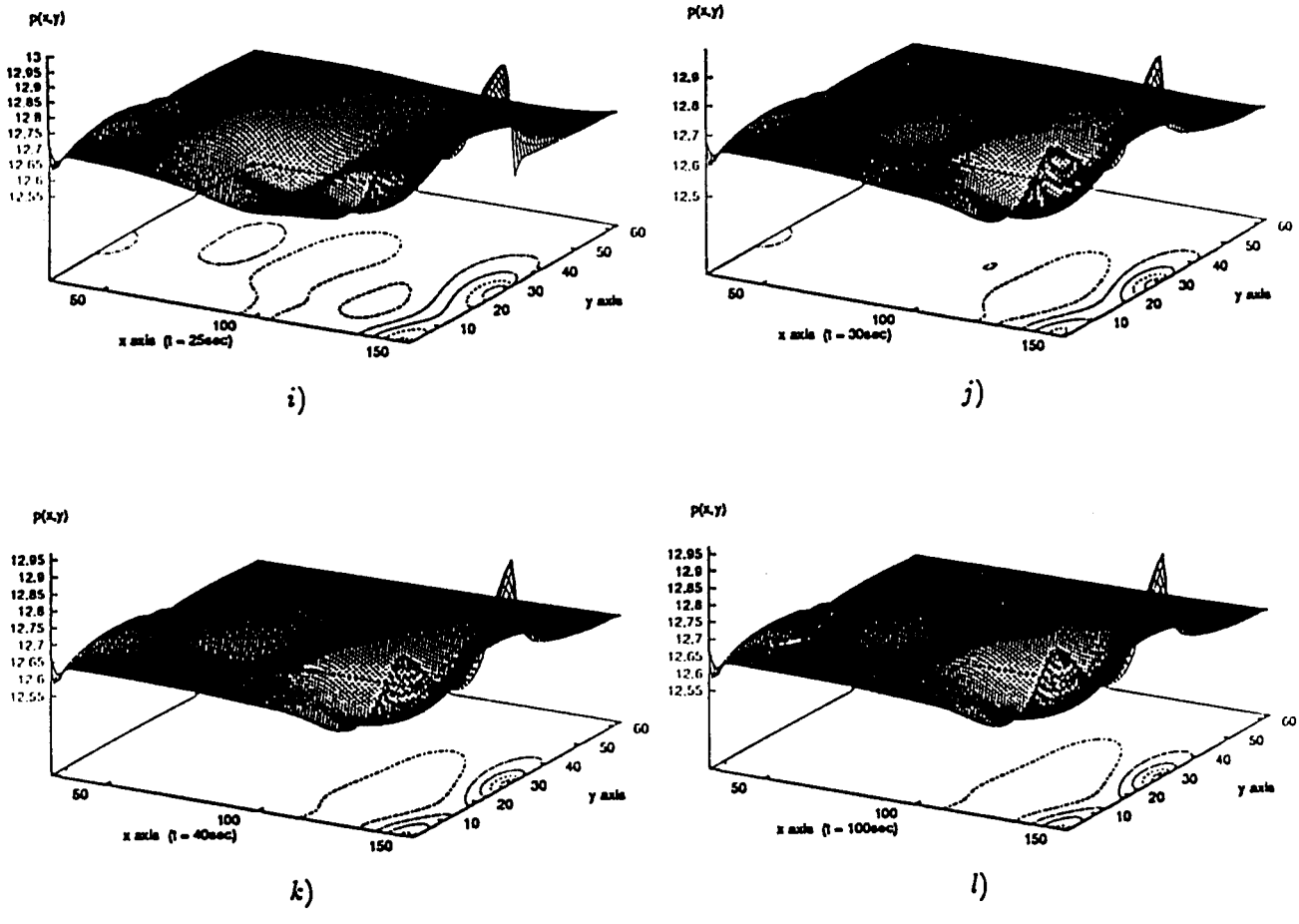

Figure 4.6: (III) $i)$ $t = 25sec$, $j)$ $t = 30sec$, $k)$ $t = 40sec$ and $l)$ $t = 100sec$

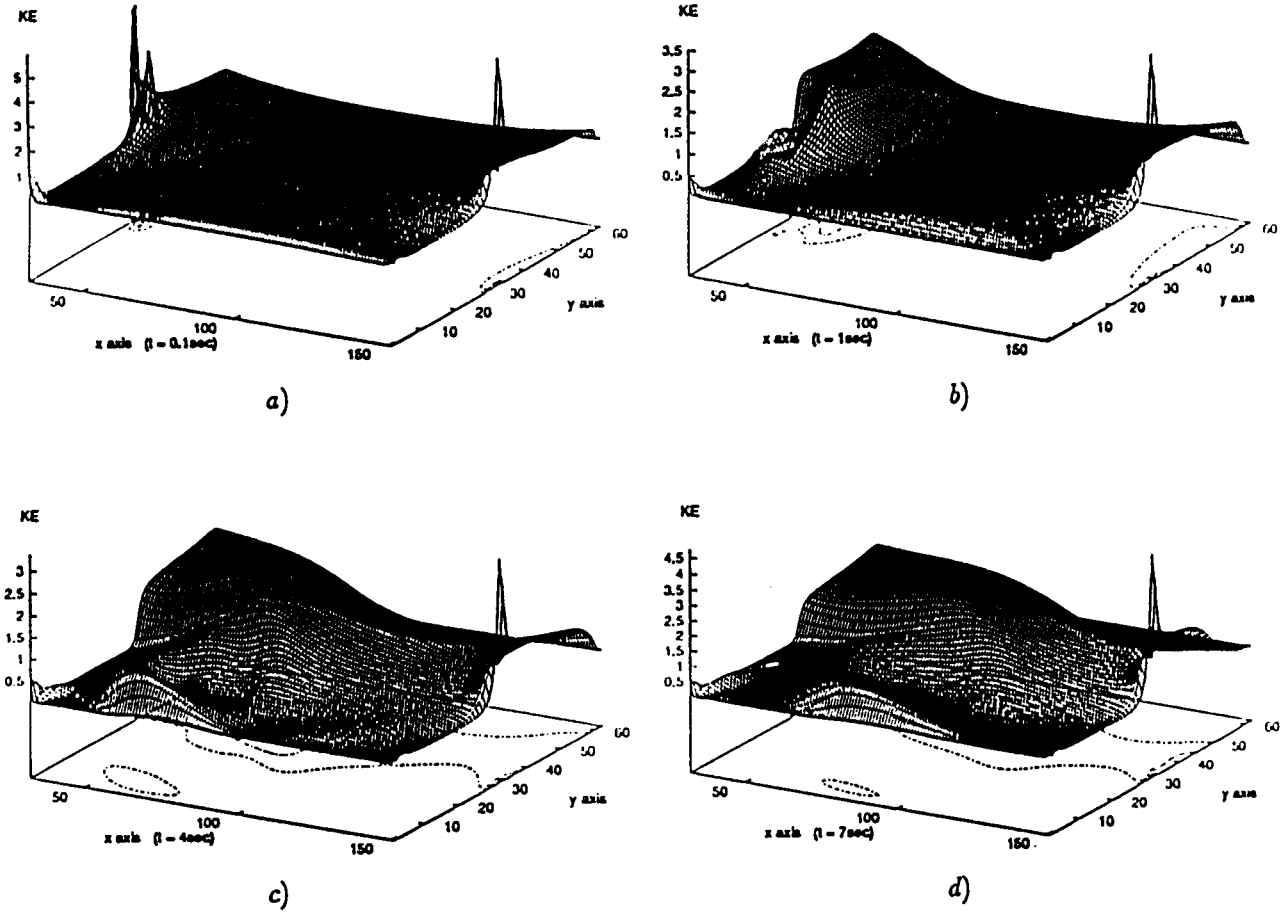

Figure 4.7: Time-development surface and contour plot of kinetic energy scaled by 10^4 ($Re = 10^3$) at (I) *a*) $t = 0.1sec$, *b*) $t = 1sec$, *c*) $t = 4sec$ and *d*) $t = 7sec$.

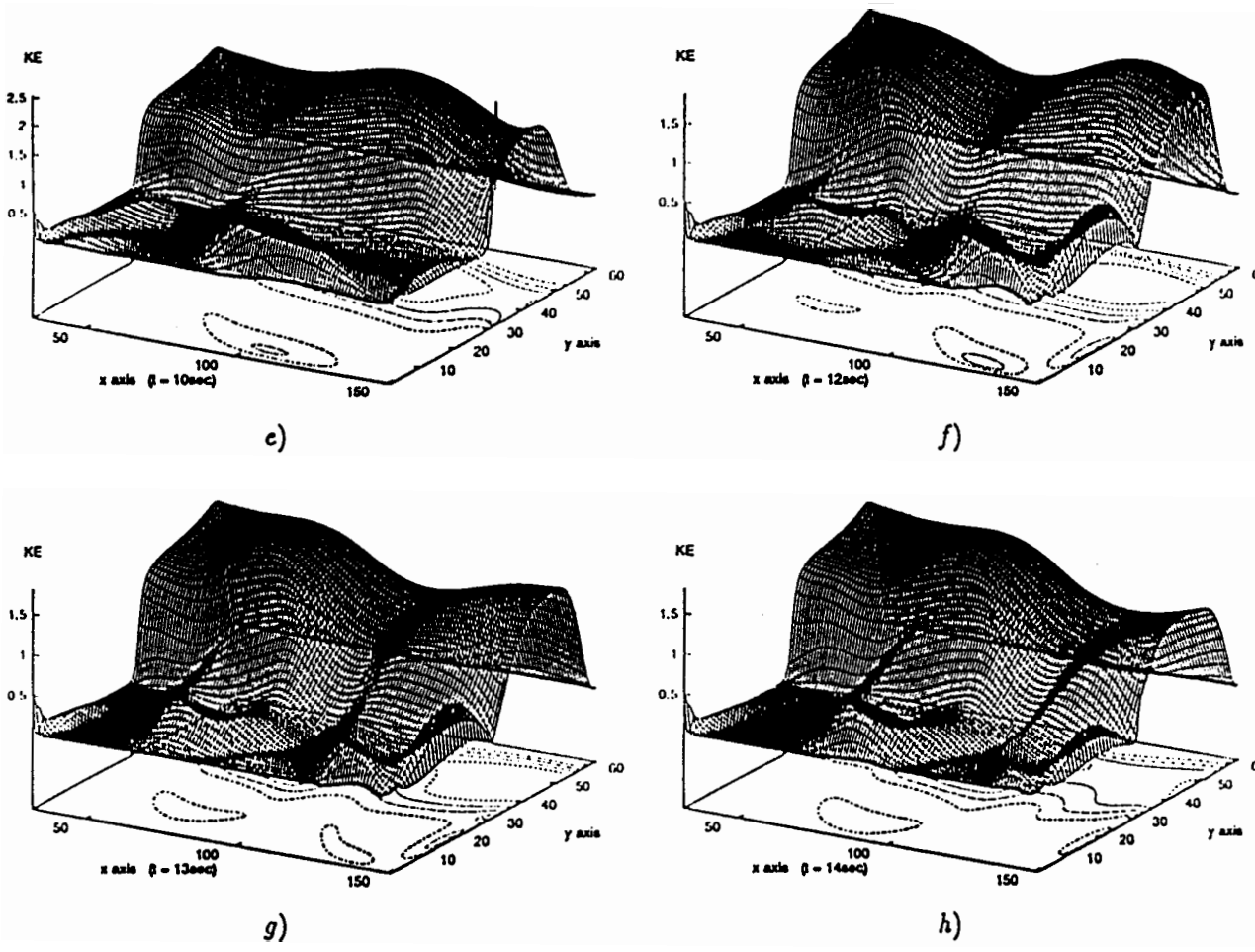

Figure 4.7: (II) $e)$ $t = 10sec$, $f)$ $t = 12sec$, $g)$ $t = 13sec$ and $h)$ $t = 14sec$.

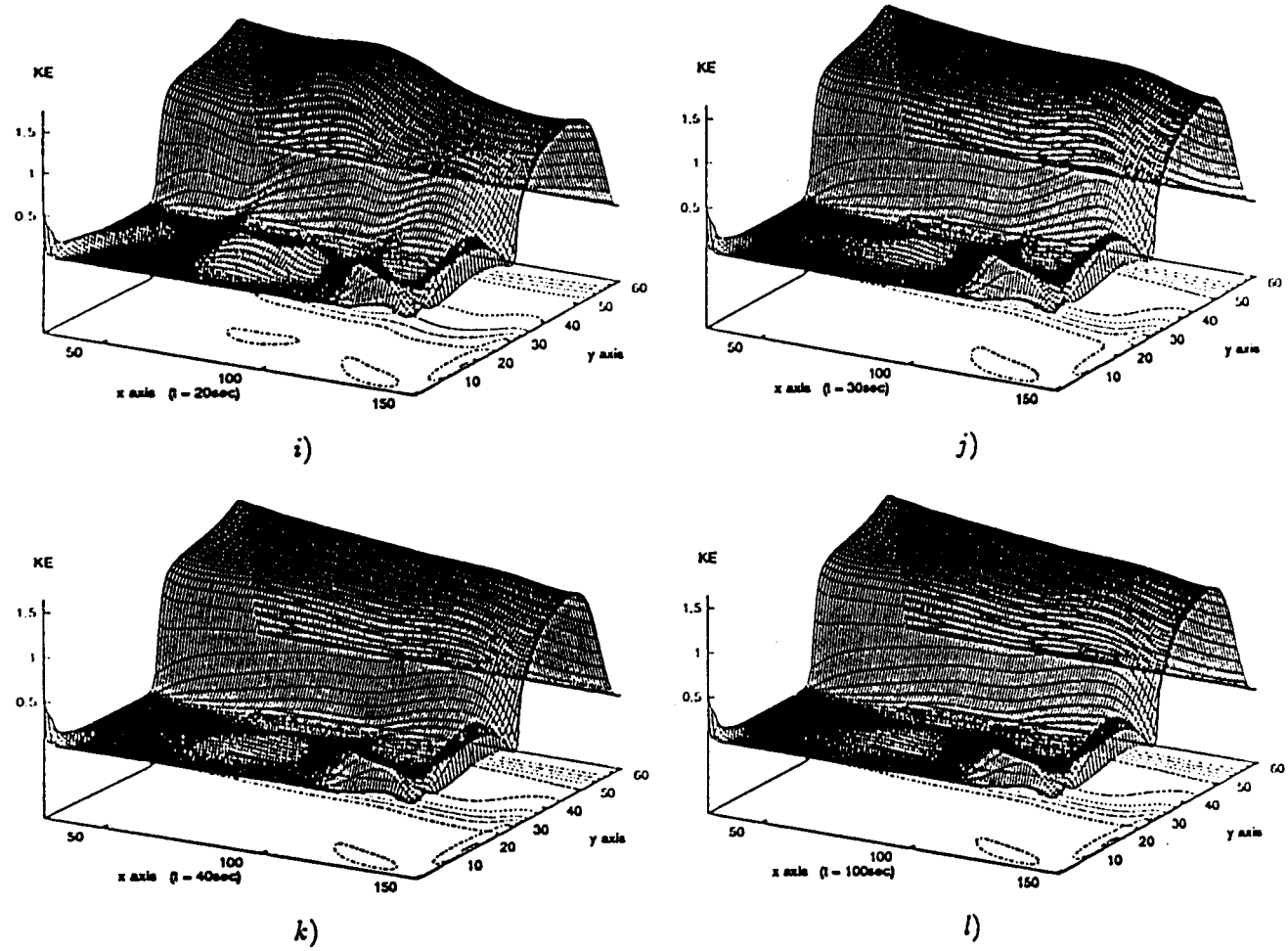

Figure 4.7: (III) i) $t = 20sec$, j) $t = 30sec$, k) $t = 40sec$ and l) $t = 100sec$.

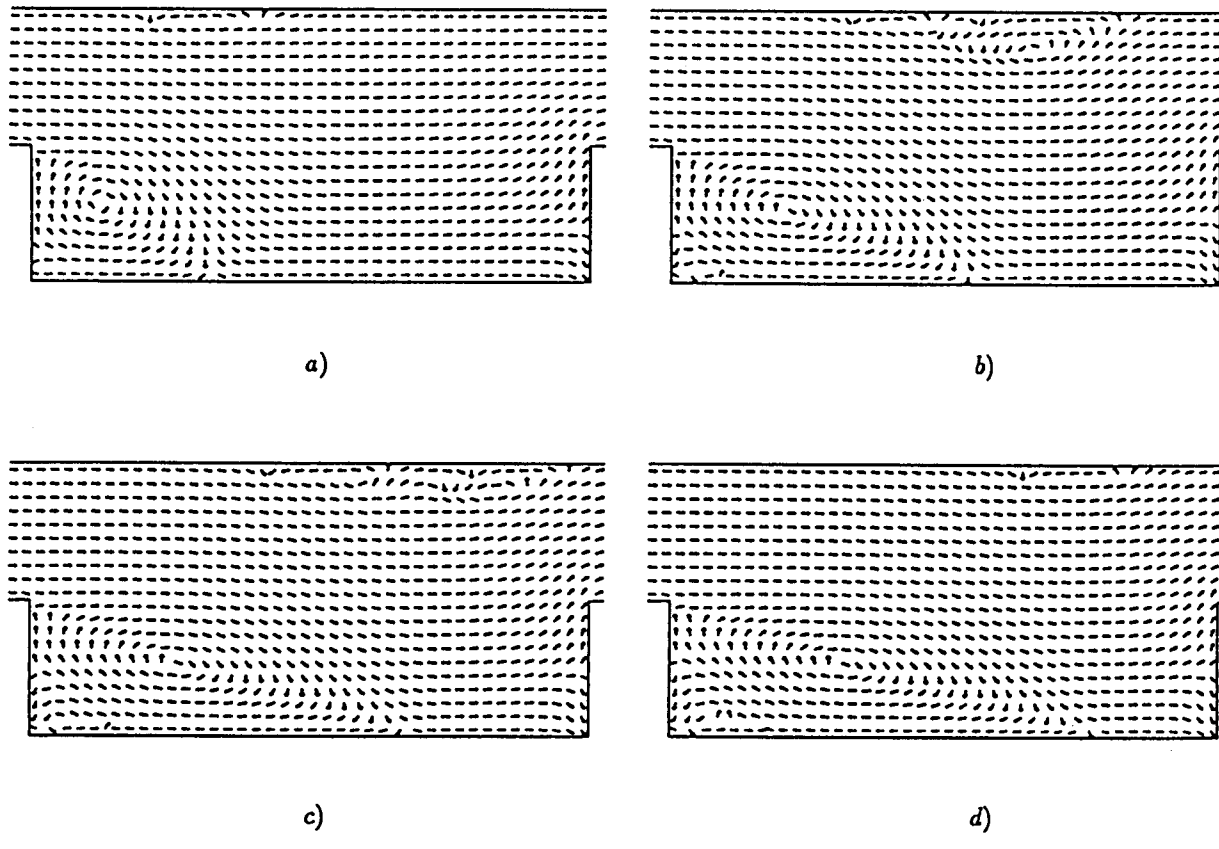

Figure 4.8: Time-development of the unsteady normalized velocity field in a channel with a cavity flow ($Re = 10^3$, coarse grid) at (I) *a*) $t = 2sec$, *b*) $t = 5sec$, *c*) $t = 8sec$ and *d*) $t = 10sec$.

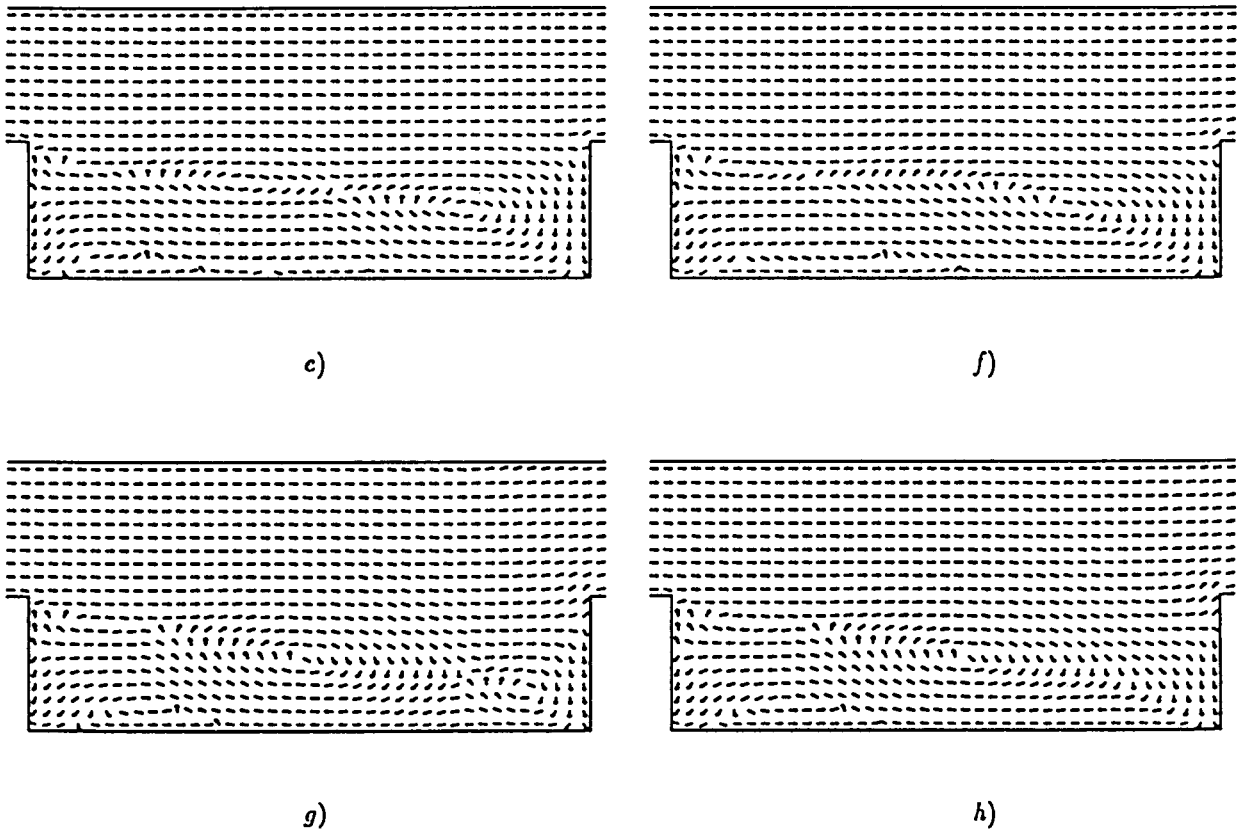

Figure 4.8: (II) e) $t = 19sec$, f) $t = 20sec$, g) $t = 25sec$ and h) $t = 26sec$.

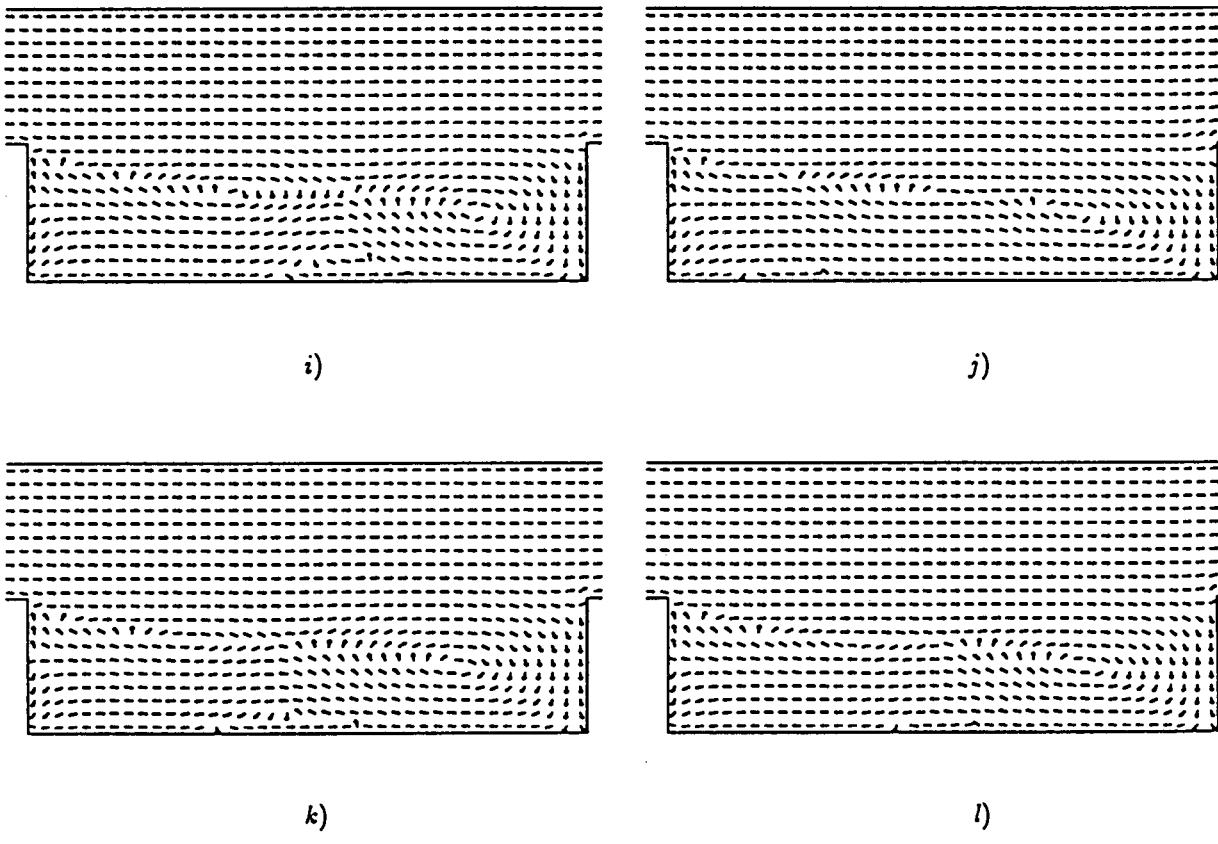

Figure 4.8: (III) $i)$ $t = 34sec$, $j)$ $t = 36sec$, $k)$ $t = 38sec$ and $l)$ $t = 50sec$.

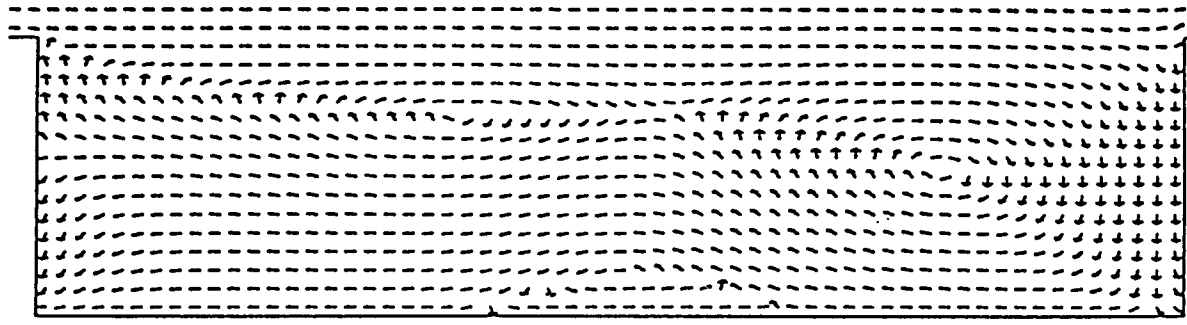

a)

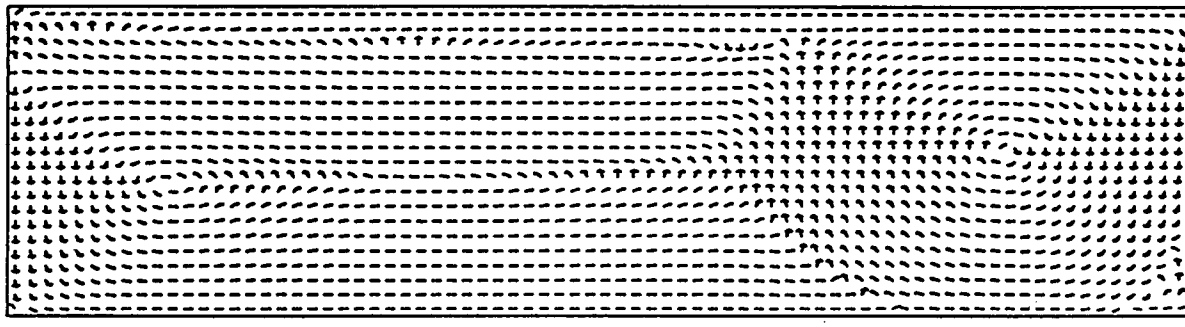

b)

Figure 4.9: Unsteady normalized velocity field ($Re = 10^3$) at $t = 100sec$ in a) the interior domain of a channel with a cavity flow and b) the driven cavity problem with $\alpha = 0.26$.

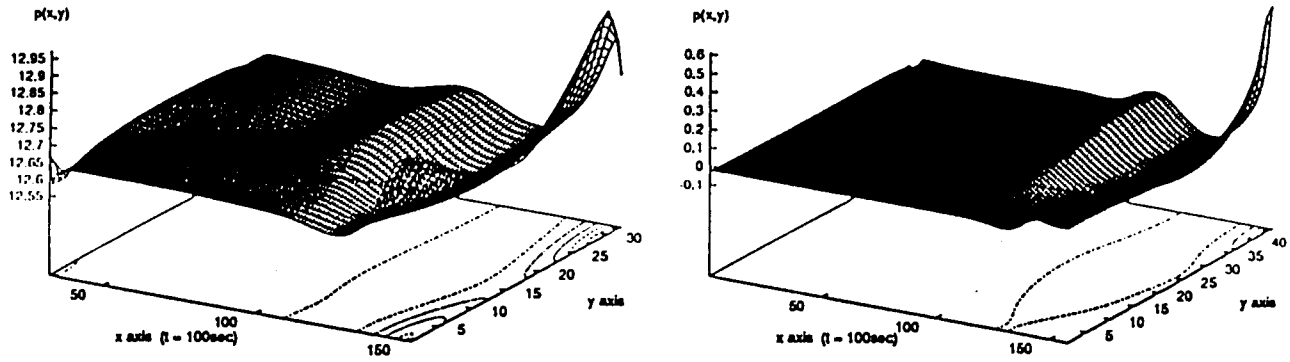

a) *b)*

Figure 4.10: Surface and contour plot of pressure ($Re = 10^3$) at $t = 100sec$ in *a)* the interior domain of a channel with a cavity flow and *b)* the driven cavity problem with $\alpha = 0.26$.

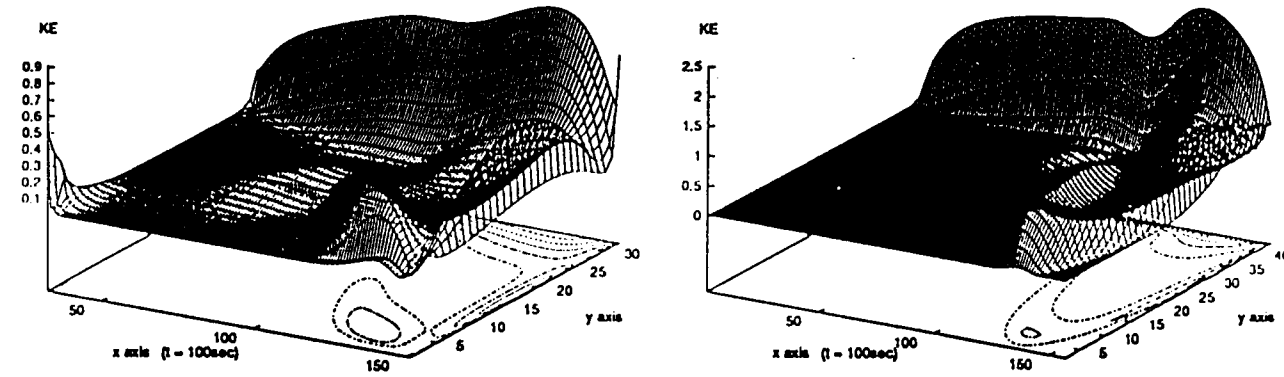

a) *b)*

Figure 4.11: Surface and contour plot of kinetic energy scaled by 10^4 ($Re = 10^3$) at $t = 100sec$ in *a)* the interior domain of a channel with a cavity flow and *b)* the driven cavity problem with $\alpha = 0.26$.

Bibliography

[1] A. S. Benjamin and V. E. Denny. On the convergence of numerical solutions for 2-D flows in a cavity at large Re. *J. Comput. Phys.*, 33:340–358, 1979.

[2] J. D. Bozeman and C. Dalton. Numerical study of viscous flow in a cavity. *J. Comput. Phys.*, 12:348–363, 1973.

[3] O. Buneman. A compact non-iterative Poisson's solver. In *Rep. 294*. Stanford University Institute for Plasma Research, Stanford, Calif., 1969.

[4] O. Burggraf. Analytical and numerical studies of the structure of steady separated flows. *J. Fluid Mech.*, 24:115–151, 1966.

[5] B. L. Buzbee, G. H. Golub, and C. W. Nelson. On direct methods for solving Poisson's equations. *SIAM J. Num. Anal.*, 7:627–656, 1970.

[6] A. J. Chorin. Numerical solution of the Navier-Stokes equations. *Math. Comput.*, 22:745–762, 1968.

[7] G. de Vahl Davis and G. D. Mallinson. An evaluation of the upwind and central difference approximations by a study of recirculating flow. *Computers and Fluids*, 4:29–43, 1976.

[8] C. A. J. Fletcher. *Computational Techniques for Fluid Dynamics.* Springer-Verlag, New York, second edition, 1991.

[9] T. B. Gatski, C. E. Grosch, and M. E. Rose. A numerical study of the two-dimensional Navier-Stokes equations in vorticity-velocity variables. *J. Comput. Phys.*, 48:1–22, 1982.

[10] U. Ghia, K. N. Ghia, and C. T. Shin. High-Re solutions for incompressible flow using the Navier-Stokes equations and a multigrid method. *J. Comput. Phys.*, 48:387–411, 1982.

[11] J. W. Goodrich, K. Gustafson, and K. Halasi. Hopf bifurcation in the driven cavity. *J. Comput. Phys.*, 90:219–261, 1990.

[12] K. Gustafson and K. Halasi. On the divergence-free (i.e. mass conservation, solenoidal) condition in computational fluid dynamics: How important is it? In C. Taylor et al., editor, *Numerical Methods in Laminar and Turbulent Flow*, page 617. (Pineridge Press, Swansea), 1983.

[13] K. Gustafson and K. Halasi. Vortex dynamics of cavity flows. *J. Comput. Phys.*, 64:279–319, 1986.

[14] K. Gustafson and K. Halasi. Cavity flow dynamics at higher Reynolds number and higher aspect ratio. *J. Comput. Phys.*, 70:271–283, 1987.

[15] K. E. Gustafson. Four principles of vortex motion. In K. E. Gustafson and J. A. Sethian, editors, *Vortex Methods and Vortex Motion*, pages 95–141. (SIAM, Philadelphia), 1991.

[16] F. H. Harlow and J. E. Welch. Numerical calculation of the time-dependent viscous incompressible flow of fluid with free surface. *Phys. Fluids*, 8:2182–2189, 1965.

[17] R. W. Hockney. A fast direct solution of Poisson's equation using Fourier analysis. *J. Assoc. Compt. Mach.*, 12:95–113, 1965.

[18] M. Kawaguti. Numerical solution of the Navier-Stokes equations for the flow in a two-dimensional cavity. *J. Phys. Soc. Japan*, 16:2307–2315, 1961.

[19] H. B. Keller. *Applications of Bifurcation Theory.* (P. H. Rabinowitz, Ed.), Accademic Press, New York, 1977.

[20] P. D. Lax. The flowering of applied mathematics in America. *SIAM Review*, 31:533–541, 1989.

[21] H. K. Moffatt. Viscous and resistive eddies near a sharp corner. *J. Fluid Mech.*, 18:1–18, 1964.

[22] F. Pan and A. Acrivos. Steady flows in rectangular cavities. *J. Fluid Mech.*, 28:643–655, 1967.

[23] R. Peyret and T. D. Taylor. *Computational Methods for Fluid Flow.* Springer-Verlag, New York, 1983.

[24] R. Phillips and M. E. Rose. Compact finite difference schemes for mixed initial-boundary value problems. *SIAM J. Num. Anal.*, 19(4):698–720, 1982.

[25] M. E. Rose. A 'unified' numerical treatment of the wave equation and the Cauchy-Riemann equations. *SIAM J. Num. Anal.*, 18(2):372–376, 1982.

[26] R. Schreiber and H. B. Keller. Driven cavity flows by efficient numerical techniques. *J. Comput. Phys.*, 49:310–333, 1983.

[27] R. Schreiber and H. B. Keller. Spurious solutions in driven cavity calculations. *J. Comput. Phys.*, 49:165–172, 1983.

[28] U. Schumann and R. A. Sweet. A direct method for the solution of Poisson's equation with Neumann boundary conditions on a staggered grid. *J. Comput. Phys.*, 20:171–182, 1976.

[29] H. L. Stone. Iterative solution of implicit approximations of multidimensional partial differential equations. *SIAM J. Num. Anal.*, 5:530–558, 1968.

[30] P. N. Swarztrauber. A direct method for the discret solution of separable elliptic equations. *SIAM J. Num. Anal.*, 11:1136–1150, 1974.

[31] P. N. Swarztrauber. The methods of cyclic reduction, Fourier analysis and the FACR algorithm for the discrete solution of Poisson's equation on a rectangle. *SIAM Review*, 19:490–501, 1977.

[32] R. A. Sweet. Direct methods for the solutions of Poisson's equation on a staggered grid. *J. Comput. Phys.*, 12:422–428, 1973.

[33] R. A. Sweet. A generalized cyclic reduction algorithm. *SIAM J. Num. Anal.*, 11:507–520, 1974.

[34] R. A. Sweet. A cyclic reduction algorithm for solving block tridiagonal systems of arbitrary dimension. *SIAM J. Num. Anal.*, 14:706–720, 1977.

[35] R. Temam. Sur l'approximation des equations de Navier-Stokes par la méthode des pas fractionnaires(II). *Arch. Ration. Mech. Anal.*, 33(5):377–385, 1969.

[36] S. Y. Tuann and M. D. Olson. Review of computing methods for recirculating flows. *J. Comput. Phys.*, 29:1–19, 1978.